



Titre: On the transferability of classical pairwise additive atomistic force field to the description of unary and multi-component systems: applications to the solidification of Al-based alloys
Title:

Auteurs: Juan-Ricardo Castillo-Sánchez, Camille Rincant, Aïmen E. Gheribi, & Jean-Philippe Harvey
Authors:

Date: 2022

Type: Article de revue / Article

Référence: Castillo-Sánchez, J.-R., Rincant, C., Gheribi, A. E., & Harvey, J.-P. (2022). On the transferability of classical pairwise additive atomistic force field to the description of unary and multi-component systems: applications to the solidification of Al-based alloys. *Physical Chemistry Chemical Physics*, 24(37), 22605-22623.
Citation: <https://doi.org/10.1039/d2cp02746a>

 **Document en libre accès dans PolyPublie**
Open Access document in PolyPublie

URL de PolyPublie: <https://publications.polymtl.ca/52143/>
PolyPublie URL:

Version: Version finale avant publication / Accepted version
Révisé par les pairs / Refereed

Conditions d'utilisation: Tous droits réservés / All rights reserved
Terms of Use:

 **Document publié chez l'éditeur officiel**
Document issued by the official publisher

Titre de la revue: Physical Chemistry Chemical Physics (vol. 24, no. 37)
Journal Title:

Maison d'édition: The Royal Society of Chemistry
Publisher:

URL officiel: <https://doi.org/10.1039/d2cp02746a>
Official URL:

Mention légale:
Legal notice:

Cite this: DOI: 00.0000/xxxxxxxxxx

On the transferability of classical pairwise additive atomistic force field to the description of unary and multi-component systems: Applications to the solidification of Al-based alloys

Juan-Ricardo Castillo-Sánchez, Antoine Rincent, Aïmen E. Gheribi, and Jean-Philippe Harvey*

Received Date
Accepted Date

DOI: 00.0000/xxxxxxxxxx

Multi-component and multiphase materials are continually being developed for electronics, aircraft, automotive, and general applications. Integrated Computational Materials Engineering (ICME) is a multiple-length scale approach that greatly benefits from atomistic scale simulations to explore new alloys. Molecular Dynamics (MD) allows to perform large-scale simulations by using classical interatomic potentials. The main challenge of using such a classical approach is the transferability of the interatomic potentials from one structure to another when one aims to study multi-component systems. In this work, the reliability of Zr, Al-Cu, Al-Cr and Al-Zr-Ti force field potentials is examined. It has been found that current interatomic potentials are not completely transferable due to the structure dependence from their parameterization. Besides that, they provide an appropriate description of unary and binary systems, notably for liquids, isotropic solids, and partially isotropic compounds. For solidification purposes, it has been found that coherent primary solidification of the FCC-phase in pure Al is highly dependent on the formalism to tune interatomic interactions. For Al-Cr alloys, the icosahedral short-range ordering (ISRO) increased by adding Cr to the melts. The different steps of solidification (formation of nuclei, effective germination of the α -Al phase and end of solidification) have been related to the evolution of the ISRO. The addition of Cr in melts prevented undercooling via icosahedral-enhanced nucleation of the α -Al phase. Precipitation of primary intermetallics in hyper-peritectic Al-Cr alloys was also tested. Contrary to classical thermodynamics predictions, α -Al phase was the primary precipitate for these alloys. This implies that Cr supersaturated the α -Al phase rather than forming intermetallic phases due to the high cooling rates.

1 Introduction

During the last decade, the exploration of innovative materials based on multi-constituent and multi-phasic metallic systems has grown considerably¹⁻⁴. For instance, High Entropy Alloys (HEAs) are a class of innovative materials made up of a large number of elemental components (more than five) with outstanding properties such as extraordinary wear strength, high hardness, phenomenal high-temperature strength, and strong corrosion resistance⁵⁻⁷. This is a result of their substantially higher mixing entropies compared to traditional alloys⁸, which energetically stabilize disordered solid solutions at high temperature. To design these materials, one must predict their thermodynamic and

elastic properties with regard to their chemical composition for some imposed temperature and pressure (or volume)^{9,10}. Experimental pilot tests to develop such complex materials result in expensive, time consuming and environmentally inefficient syntheses, machining and testing experiments. In this context, numerical physics could play an important role to overcome such challenges^{11,12}. Computational quantum mechanical modeling methods, notably those based on Density Functional Theory (DFT), have the highest predictive abilities since they explicitly consider the effect of the electronic structure of individual atoms on the energetic behavior of the considered system^{13,14}. Unfortunately, these calculations are limited to hundreds of atoms with the actual available computational resources¹⁵, resulting in an overall deviation of the simulated thermodynamic, thermal and volumetric properties when compared to actual bulk materials. These materials often present metallurgical features such as grains and

Centre for Research in Computational Thermochemistry (CRCT), Department of Chemical Engineering, Polytechnique Montréal, C.P. 6079, Succursale "Downtown", Montréal, Québec H3C 3A7, Canada. E-mail: jean-philippe.harvey@polymtl.ca

grain boundaries at a much larger scale (i.e. micron scale).

Simulations based on Equilibrium Molecular Dynamics (EMD) are nowadays widely employed to describe the equilibrium and dynamic properties, as well as thermal transport properties of metallic systems^{16–18}. MD typically cannot rigorously describe the electronic density surrounding individual atoms because of the simplified nature of the interatomic potential functions used in these simulations. Therefore EMD simulations cannot be as precise as DFT-based calculations when it comes to the evaluation of energetic properties, especially when metallic interactions are involved. Instead, EMD is based on a force field function depending mainly on interatomic distances between atoms constituting the system under study, which lowers the computational cost compared to DFT¹⁹. The accuracy of EMD in predicting the material's thermodynamic properties strongly depends on the reliability of the force field formulated to describe the different contributions of the interactions between each atom of the studied supercell. For metallic systems, there exists a large variety of analytical force field formalisms to modulate the interatomic interactions; for instance, the Embedded Atom Method (EAM)²⁰, the Finnis–Sinclair (EAM-FS)²¹, Second-Moment Approximation of the Tight-Binding scheme (TB-SMA)²² and the Modified Embedded Atom Method (MEAM) potential²³. The original MEAM formalism was extended in order to consider the second nearest-neighbor interactions, which is called the Second Nearest-Neighbor Modified Embedded-Atom-Method (2NN-MEAM)²⁴. This formalism is widely used in the recent literature, especially for metallic systems, due to its good predictive abilities. Remarkably, a potential database is available for almost all pure metals^{25–30}. Recent research on the description of binary³¹ and ternary^{32–34} systems is paving the way towards the numerical exploration of high entropy alloys of tremendous interest for various applications. In particular, those based in Al-Cu-Fe-Ni-Mn-Cr-Ti-Zr-X (X=others important metals) systems. The advantage of the MEAM potential is that only a few set of parameters is needed for its modeling, this allows to create homogeneous databases.

The parameterization strategy of the force field using the 2NN-MEAM formalism has been explained in detail by Lee and Baskes²⁴. Elements are commonly parameterized from well-known crystallographic structures (such as face-centered cubic FCC, body-centered cubic BCC, and hexagonal close-packed HCP structures) at standard conditions of pressure and temperature (10⁵ Pascal and 298.15 K)²⁶. For binary systems, force field parameters can be directly obtained from first-principles calculations. Required information includes: (a) the strength of the energetic interactions at the ground state (obtained via the sublimation energy), (b) the bulk modulus, (c) equilibrium atomic volume from a reference crystal structure, (d) defect formation energies, and (e) elastic constants of some reference structures. The energetic description of binary systems can supposedly be obtained from the selection of any reference structure (i.e. regardless of the composition ratio of the two elements involved) as these interatomic potentials aimed at being universal functions. However, we found here that it is preferable to relate the reference structure to the one of a thermodynamically stable intermetallic compound observed in a measured phase diagram.

In this case, the parameterization procedure is based on experimentally measured properties³⁵, which may not be self-consistent with DFT-based simulations. In some cases, the reference structure is related to a metastable compound, such as the selection of the Al₃Li-Li₂ reference structure in the energetic description of the Al-Li system³⁶, or to a simple binary structure, such as the rock-salt NaCl structure (B1) in the Al-Cu parameterization with the 1NN-MEAM formalism^{37,38}. In the case of the MD study of the Al-Li system, the specific exploration of the energetic behavior of the Li₂ metastable phase justifies the selection of the reference structure³⁶. In fact, any hypothetical reference structure can be used if first-principle calculations are available in the literature. One has to remember that the chosen reference structure modulates the various pair fractions to be accounted for in the evaluation of the internal energy of the system. This is a critical aspect to consider when tuning the strength of heterogeneous A-B energetic interactions. As an example, the fraction of A-B first nearest neighbor pairs in a hypothetical AB - B2 ordered structure is equal to one. In this case, only the A-B interactions influence the energetic behavior of the reference structure (in the 1NN approximation). The isotropy of the reference structure is another major aspect to consider when optimizing an interatomic potential. In principle, an isotropic reference structure is more suitable for describing liquid solutions, while most stable solid phases are not. In this context, DFT is a wonderful tool because it allows the access to the energetic behavior of isotropic structures of metastable phases and liquid solutions as well^{39–41}.

There is no strict methodology to judge the accuracy and transferability of a given interatomic potential. Nonetheless, it should be able to reproduce key equilibrium properties of specific solid structures, in particular, cohesive energy, lattice constants, elastic constants, surface energy, and energetics of defects, among others. This should be coupled with a satisfactory thermodynamic description of enthalpy of mixing, thermal conductivity, and other properties of liquids if reference data are available. In principle, a suitable force field is transferable from one structure to another as well as for the description of multicomponent solutions where many unary and binary interactions are simultaneously present. Most of the force field potentials are currently based on pairwise interactions⁴². Many-body interactions can partially be captured through a screening function in sophisticated formalisms, such as in the MEAM modeling. The three-body screening function in the 2NN-MEAM considers the effect of a third atom on the interaction between a pair of atoms⁴³. Such approximations have limitations for multi-component systems as the chemical surrounding of a given atom (or pair) may vary. From continuum thermodynamics, it is well-established that ternary and quaternary energetic interaction corrections are needed to properly describe the enthalpy of mixing of multi-component systems when experimental data are available^{44,45}. This brings us to the following questions: a) How accurately can we describe the energetic behavior of multi-component metallic systems using the parameterization of two-body interactions from unary and binary systems only? and b) How is the choice of the reference structure impacting the prediction of thermodynamic properties of multi-component systems?

Conventionally, the classical EAM formalism requires a signifi-

icant number of empirical parameters to accurately describe a specific condensed phase. However, this large number of parameters does not necessarily ensure that the interatomic potential will be transferable to liquid and solid solutions. Srinivasan et al.⁴⁶ recently compared the predictive strength of two popular interatomic potentials used to perform MD simulations of metals. They found that for the binary Ni-Ti system, the 2NN-MEAM potential outperforms the EAM-FS potential. The 2NN-MEAM potential was able to estimate transformation strain, Young's modulus, lattice constants, and elastic constants with better accuracy than the EAM-FS⁴⁶. Moreover, up to a thousand parameters are needed for some EAM interatomic potentials, whilst MEAM formalism is based on a simpler and more reliable parameterization which is believed to ensure a better transferability from one system to another.

Large-scale molecular dynamics simulations have become relevant to studying solidification in metals. Hou et al.⁴⁷ studied the effect of the cooling rate in pure aluminum. They worked with simulation boxes of 1 048 576 atoms and used an embedded atoms method (EAM) potential⁴⁸ to describe the Al-Al interactions. They worked with cooling rates between 0.1 and 10 K/ps. They found that the fastest cooling rate (10 K/ps) promoted the formation of metallic glasses with short-range icosahedral ordering. Simulation boxes solidified into the FCC and HCP phases for slower cooling rates (≤ 4 K/ps). Crystallization of the metastable HCP phase was associated with twinning. Zhang et al.⁴⁹ used cubic simulation boxes of 3 456 000 atoms to study the rapid solidification in pure iron melts. They used the embedded atoms method (EAM) potential⁵⁰ to describe the iron interatomic interactions and used cooling rates between 0.09 5K/ps and 9.5 K/ps. They concluded that the icosahedral ordering was promoted in undercooled melts by increasing the cooling rate. They reported a critical cooling value of 4 K/ps for glass transition. i.e., above this value, the icosahedral-like configurations were dominant and led to the formation of amorphous structures. Below the critical value, crystalline structures were obtained. These studies provided insights into the solidification mechanisms of pure systems. However, solidification simulations for multicomponent systems are required to design new alloy. Harvey & Asimow⁵¹ pointed out some of the current limitations of MD simulations for the thermodynamic description of silicate melts, which are related to the time and length scales as well as the fundamental description of interatomic interactions. This study aims to evaluate the effect of such limitations on the solidification of Al-based alloys.

In this work, the transferability of a series of interatomic potentials has been evaluated for specific applications linked to the solidification of metallic systems. Firstly, the impact of using two distinct reference allotropes (i.e. HCP and BCC) on the energetic description of pure liquid Zr is explored. Secondly, the effect of the selection of a given binary reference structure on the prediction of the phase stability in the Al-Cu system is analyzed using three different metastable compounds as reference structures (i.e. Al₃Cu-L1₂, Cu₃Al-L1₂ and AlCu-BCC with self-consistent data obtained from DFT calculations). Solidification of pure Al is studied using two of the most popular models in MD (i.e. the EAM.FS and 2NN-MEAM formalism). Finally, the transferability of classical

pairwise interatomic potentials is evaluated for the icosahedral-enhanced nucleation of the FCC-phase⁵² in Al-Cr alloys.

2 Force field development

The Second Nearest-Neighbor Modified Embedded-Atom-Method (2NN-MEAM)²⁴, commonly denoted only as MEAM, was used to describe the strength of the interatomic interactions in our work. This formalism is integrated as a package of the popular LAMMPS code⁵³ for Equilibrium Molecular Dynamic (EMD) simulations. The MEAM potential can accurately capture the directionality of metallic bonds due to the implicit angle-dependent terms⁴⁶. Total energy with the MEAM formalism is defined by two contributions: an embedding function (F) and a pair potential function (ϕ_{ij}):

$$E = \sum_i \left\{ F(\bar{\rho}_i) + \frac{1}{2} \sum_{i \neq j} \phi_{ij}(R_{ij}) \right\} \quad (1)$$

Where $\bar{\rho}_i$ is the background electron density at the site of the i -th particle and R_{ij} is the distance between particles i and j . The embedded function is given by:

$$F(\bar{\rho}_i) = AE_c \frac{\bar{\rho}_i}{\rho^0} \ln \left(\frac{\bar{\rho}_i}{\rho^0} \right) \quad (2)$$

Where A is a specific parameter of the MEAM formalism. E_c is the cohesive energy and ρ^0 is the background electron density of the reference structure. Background electron density is related to the angular dependent partial electron densities, $\rho_i^{(k)}$, and to the weighting parameters, $t(k)$, via equations 3 and 4. $t(1)$, $t(2)$, and $t(3)$ are respectively adjusted according to the relevance of the p, d and f orbitals⁵⁴.

$$\bar{\rho}_i = \rho_i^{(0)} \frac{2}{1 + e^{-\Gamma_i}} \quad (3)$$

$$\Gamma_i = \sum_{k=1}^3 t^{(k)} \left(\frac{\rho_i^{(k)}}{\rho_i^{(0)}} \right)^2 \quad (4)$$

The atomic electron density is introduced as an exponentially-decaying function with respect to distance^{25,54}:

$$\rho^{a(h)}(R) = e^{-\beta^{(h)} \left(\frac{R}{r_e - 1} \right)} \quad (5)$$

$\beta^{(h)}$ are adjustable parameters, and r_e is the nearest neighbor distance of the reference structure. For more details about the partial electron density expressions related to $\rho^{a(h)}(R)$, the reader is referred to the force field model of Lee et al.²⁵.

The pair potential function is estimated using the following equation:

$$\phi_{ij}(R_{ij}) = \psi(R_{ij}) + \sum_{n=1} (-1)^n (Z_2 S / Z_1)^n \psi(a^n R_{ij}). \quad (6)$$

Where Z_1 and Z_2 are the number of first and second nearest-neighbor atoms, respectively. a is the ratio between the second and first nearest neighbor distances, S is a screening function on the second nearest-neighbor interactions and $\psi(R_{ij})$ is pair function obtained with the following equation :

$$\psi_{ij}(R_{ij}) = \frac{2}{Z_1} \{ E^n(R_{ij}) - F[\bar{\rho}^0(R_{ij})] \} \quad (7)$$

The total energy per atom, $E^u(R_{ij})$, is obtained from the universal equation of state⁵⁵:

$$E^u(R_{ij}) = -E_c \left(1 + a^* + da^{*3}\right) e^{-a^*} \quad (8)$$

With $a^* = \alpha(R_{ij}/r_e - 1)$ and $\alpha = \left(\frac{9B\Omega}{E_c}\right)^{1/2}$. Where d is an adjustable parameter. E_c is the cohesive energy, r_e is the equilibrium distance, B is the bulk modulus, and Ω is the equilibrium atomic volume of the reference structure.

The optimized parameters to describe the pure metal pairwise interactions via the 2NN-MEAM formalism are presented in Table 1. They were primarily taken from Kim and Lee studies^{25–27}, except for the BCC-based potential for Zr, which was parameterized in this work.

As previously stated, the parameterization of a binary interatomic potential using the 2NN-MEAM formalism relies on the selection of a binary reference structure. Popular Molecular Dynamics programs such as LAMMPS and KISSMD can support different reference structures, essentially, the rock-salt NaCl structure (B1), and the BCC-like CsCl structure (B2), the AuCu₃-prototype (L1₂), among others. In ideal conditions, it is preferable to associate the binary reference structure with a stable intermetallic compound as it ensures the most accurate description of a given binary interaction. However, this cannot always be achieved as the crystal structure of the stable intermetallic compound may not be supported by the classical MD package or simply because they may not be a stable binary compound for that particular binary system. A sound strategy to properly select the reference structure from first-principle calculations is to compare its enthalpy of formation with the one computed by classical thermodynamics packages such as FactSage which exploit CALPHAD-based thermodynamic databases (which are built using a collection of critically assessed experimental data found in the literature).

Figure 1 shows the enthalpy of formation (refs.: Al-FCC and Cu-FCC) for several reference structures coming from DFT calculations at 0 K (black spheres)⁵⁶ compared with the enthalpy of formation at 298.15 K of the solid system computed with the FTlite database⁵⁷ (black line). It can be observed that the enthalpy of formation calculate via DFT for Al₂Cu (I4/mcm), AlCu (C2/m), Al₄Cu₉, AlCu₃ (L1₂) and AlCu₃ (IA/mcm) structures are in excellent agreement with the thermodynamic calculations. From this list of compounds, only the AlCu₃ (L1₂) reference structure is supported by LAMMPS⁵³ and KISSMD³⁵ when using the 2NN-MEAM. Therefore, this reference structure was used for the construction of one force field model in this work (see table 2). AlCu₃ (L1₂) and AlCu (B2) DFT references were also considered to parametrize the Al-Cu interactions of two additional models (Table 2). It is to be noted that none of these compounds are reported as stable phases in the equilibrium Al-Cu phase diagram. Out of these three reference structures, the AlCu₃ (L1₂) has the closest enthalpy of formation to the CALPHAD curve (obtained from computational thermochemistry). The enthalpy of mixing in the liquid state (refs.: Al-liq. and Cu-liq.) calculated with the FTlite database is also presented in Figure 1. The minimum value on this enthalpy of mixing curve is shifted towards a Cu molar

fraction of 0.6 (red curve in Figure 1), which represents a modelling challenge in both EMD and computational thermochemistry. This shift implies that a specific local ordering is established in the liquid phase, which appears to be also present in the solid state.

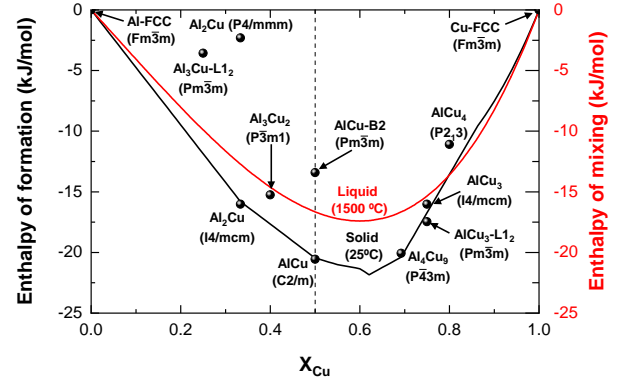


Fig. 1 Enthalpy of formation of different compounds from DFT calculations (black spheres)⁵⁶ compared with the solid (25°C) and liquid (1500°C) enthalpies of formation computed to the critically assessed value⁵⁷.

The Cr-Al and Al-Zr energetic interactions were also tuned from equilibrium reference structures at 0K obtained via DFT calculations⁵⁶. A hypothetical Zr₃Ti-L1₂ reference structure was selected for the parameterization of the Zr-Ti interaction via the 2NN-MEAM formalism (Table 2). The enthalpy of formation for the Zr₃Ti-L1₂ reference was set to a value of +0.04eV (i.e. close to zero), which was determined by fitting the liquid enthalpy of mixing with a ± 1 kJ/mol margin of error compared to the critically assessed value (Figure 2). This virtually zero enthalpy of formation leads to an ideal solution behavior for this system. This is consistent with the current phase diagram calculated from the

Table 1 2NN MEAM potential parameter sets for pure Al, Zr, Cu, Cr and Ti. The units of the cohesive energy E_c , equilibrium nearest-neighbor distance r_e , and bulk modulus B are eV, Å and 10^{12} dyne/cm², respectively. The reference structure for Al and Cu is fcc, bcc for Cr, hcp for Ti and two references for Zr, i.e. bcc and hcp.

	E_c	r_e	B	A	$\beta^{(0)}$	$\beta^{(1)}$	$\beta^{(2)}$	$\beta^{(3)}$	$\iota^{(1)}$	$\iota^{(2)}$	$\iota^{(3)}$	C_{min}	C_{max}	d
Al ²⁶	3.36	2.860	0.794	1.16	3.20	2.6	6.0	2.6	3.05	0.51	7.75	0.49	2.80	0.05
Zr-BCC	6.29	3.100	0.900	0.95	3.30	1.0	1.0	1.0	5.80	-0.35	-1.30	0.25	2.80	0.00
Zr-HCP ²⁷	6.36	3.200	0.970	0.68	2.45	1.0	3.0	2.0	6.30	-3.30	-10.00	1.00	1.44	0.00
Cu ²⁶	3.54	2.555	1.420	0.94	3.83	2.2	6.0	2.2	2.72	3.04	1.95	1.21	2.80	0.05
Cr ²⁵	4.10	2.495	1.900	0.42	6.81	1.0	1.0	1.0	0.30	5.90	-10.40	0.78	2.80	0.00
Ti ²⁷	4.87	2.920	1.100	0.66	2.70	1.0	3.0	1.0	6.80	-2.00	-12.00	1.00	1.44	0.05

Table 2 Optimized 2NN-MEAM potential parameters for individual binary systems. The units of the cohesive energy E_c , equilibrium nearest-neighbor distance r_e , and bulk modulus B are eV, Å and 10^{12} dyne/cm², respectively.

	Cu-Al	Cu-Al	Cu-Al	Cr-Al	Al-Zr	Zr-Ti
Ref. structure	Cu ₃ Al - L1 ₂	CuAl - BCC_B2	CuAl ₃ - L1 ₂	CrAl ₃ - L1 ₂	Zr ₃ Al - L1 ₂	Zr ₃ Ti - L1 ₂
ΔE_c (eV)	-0.181	-0.140	-0.037	-0.115	-0.296	0.040
r_e	2.596	2.596	2.775	2.757	3.105	2.981
B	1.29	1.39	0.91	1.22	1.01	1.03
C_{min} (A-B-A)	0.09	1.21	1.21	0.25	1.00	1.00
C_{min} (B-A-B)	0.09	0.81	0.49	0.49	1.00	1.00
C_{min} (A-A-B)	0.09	0.81	0.81	0.25	0.81	1.00
C_{min} (A-B-B)	0.09	0.81	0.81	0.36	0.81	1.00
C_{max} (A-B-A)	1.44	2.80	2.80	2.80	1.44	2.80
C_{max} (B-A-B)	1.44	2.80	2.80	2.80	1.44	2.80
C_{max} (A-A-B)	1.44	2.80	2.80	2.80	2.80	2.80
C_{max} (A-B-B)	1.44	2.80	2.80	2.80	2.80	2.80
d	$0.75d^{Cu} + 0.25d^{Al}$	$0.50d^{Cu} + 0.50d^{Al}$	$0.25d^{Cu} + 0.75d^{Al}$	$0.25d^{Cr} + 0.75d^{Al}$	$0.75d^{Zr} + 0.25d^{Al}$	$0.75d^{Zr} + 0.25d^{Ti}$
ρ_0	$\rho_0^{Cu} = \rho_0^{Al} = 1$	$\rho_0^{Al} = \rho_0^{Cr} = 1$	$\rho_0^{Cu} = \rho_0^{Al} = 1$	$\rho_0^{Al} = \rho_0^{Cr} = 1$	$\rho_0^{Al} = \rho_0^{Zr} = 1$	$\rho_0^{Al} = \rho_0^{Ti} = 1$

FTlite database of FactSage⁵⁷. This phase diagram, presented in Figure S1 (Supplementary Information), shows that Ti and Zr are completely miscible in all the stable solutions (i.e. HCP, BCC and liquid). The energetics of the selected reference structures (black triangle and spheres in Figure 3) for the Al-Cr, Al-Zr and Ti-Zr interactions were compared with the CALPHAD curves at 298.15 K (blue, green and red solid lines), which were computed with the FTlite database⁵⁷. Overall, this comparison confirms that the selected reference structures are consistent with computational thermochemistry calculations.

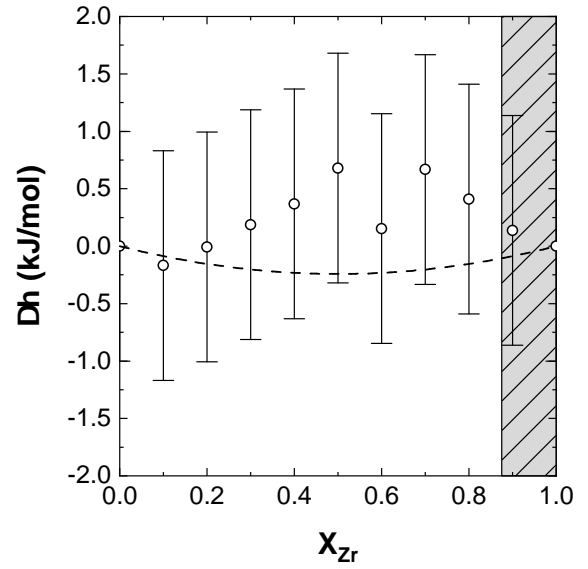


Fig. 2 Molar enthalpy of mixing for liquid Ti-Zr. Open circles and line are the thermodynamic data calculated with MD at T= 2000 K. Dashed line are results at 2000 K from classical thermodynamics performed in FactSage⁵⁷. Shaded grey zone correspond to the meta-stability zone of the liquid at 2000K.

Screening parameters, C_{min} and C_{max} , for the modeling of the ternary Al-Zr-Ti system using the MEAM formalism, are presented in Table 3. Finally, the MEAM interatomic potential developed by Kim et al. (2016)⁵⁸ was used to describe the Al-Ti interactions needed within the Al-Zr-Ti system.

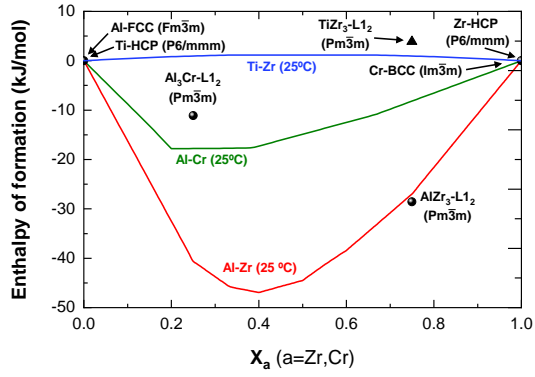


Fig. 3 Enthalpy of formation of different compounds from DFT calculations (black spheres)⁵⁶, and the hypothetical Zr_3Ti-L_{12} reference (black triangle) compared with the solid enthalpy of formation at 25°C computed to the critically assessed value⁵⁷.

Table 3 Default value for 2NN-MEAM potential parameters of the Ti-Zr-Al ternary system.

Parameter	Selected value
$C_{min,max}^{Ti-Al-Zr}$	$\left(\frac{1}{2}\sqrt{C_{min,max}^{Ti-Al-Ti}} + \frac{1}{2}\sqrt{C_{min,max}^{Zr-Al-Zr}}\right)^2$
$C_{min,max}^{Ti-Zr-Al}$	$\left(\frac{1}{2}\sqrt{C_{min,max}^{Ti-Ti-Al}} + \frac{1}{2}\sqrt{C_{min,max}^{Zr-Zr-Al}}\right)^2$
$C_{min,max}^{Zr-Ti-Al}$	$\left(\frac{1}{2}\sqrt{C_{min,max}^{Zr-Zr-Al}} + \frac{1}{2}\sqrt{C_{min,max}^{Ti-Ti-Al}}\right)^2$

3 Simulation details

Molecular Dynamics simulations were performed using the LAMMPS code⁵³. Temperature and pressure were controlled by a Nose-Hoover thermostat and barostat^{59–62}. Periodic boundary conditions were used for the three Cartesian directions. Newton's equation of motion was solved by means of the velocity-Verlet method⁶³ using a time step of 1 fs. Structural analysis was carried out with OVITO software⁶⁴, using the Common Neighbor Analysis (CNA)⁶⁵ and the Polyhedral Template Matching (PTM) reported by Larsen et al.⁶⁶. Quantification of the local structure was performed with the Radial Distribution Function (RDF). It describes the probability of finding atoms as a function of the distance from a reference particle compared to the probability of finding an atom at these same interdistances in an ideal gas. It is mathematically defined by the following equation⁶⁷:

$$g_{ij}(r) = \frac{\langle \sum \delta_{ij}(r - r_{ij}) \rangle}{4r\pi^2\rho_0} \quad (9)$$

where r_{ij} is the distance between atoms i and j , ρ_0 is the mean number density. The total RDF is related to the partial RDF by the following expression:

$$g(r) = x_\alpha^2 g_{\alpha\alpha}(r) + 2x_\alpha x_\beta g_{\alpha\beta}(r) + x_\beta^2 g_{\beta\beta}(r) \quad (10)$$

Where x_α and x_β are the molar fractions of the species α and β . $g_{\alpha\alpha}$, $g_{\alpha\beta}$ and $g_{\beta\beta}$ are the partial functions obtained with equation 9.

Bond-Angle Distribution Function or Angular Distribution Function (ADF), quantifies the probability of forming an angle θ from two nearest neighbours of a reference central atom. It is given by the following equation⁶⁸:

$$g(\theta) = 16\pi^2 \int_0^{D_1} \int_0^{D_1} R_1^2 R_2^2 g(R_1) g(R_2) g_3(R_1, R_2, \theta) dR_1, dR_2 \quad (11)$$

Where D_1 is the maximum distance between a central atom and its first nearest neighbor atoms (first minimum on the RDF) and $g_3(R_1, R_2, \theta)$ is a triplet correlation function.

3.1 Thermodynamic property evaluation

The specific (molar) enthalpy of mixing (Δh_{mix}) of liquid solutions at a given temperature was calculated using the following equation:

$$\Delta h_{mix}^{liq.} = h_{liq.} - \sum x_i h_i \quad (12)$$

Where $h_{liq.}$ is the equilibrium enthalpy of the molten alloy, x_i and h_i are respectively the molar fraction and the molar enthalpy of the pure liquid of constituent " i " at the same temperature and pressure conditions.

The molar enthalpy of formation at 0 K (Δh_f^{0K}) of solid phases was computed by the following equation:

$$\Delta h_f^{0K} = h_{comp}^{0K} - \sum x_i h_i^{SER-0K} \quad (13)$$

In eq. 13, h_{comp}^{0K} is the molar enthalpy of the compound, and x_i

is the molar fraction of the " i " component within the solid phase. In all our calculations, the enthalpy of the solid structure at 0 K was obtained at a null pressure via a volume minimization of the studied supercell. Finally, h_i^{SER-0K} refers to the enthalpy of pure element i evaluated at 0 K under its Standard Element Reference state (defined as SER-0K).

3.2 MD simulations of solidification and precipitation

The MD simulation for the solidification of pure aluminum and of the icosahedral-enhanced nucleation of the FCC-phase of Al-Cr alloys presented in section 4 were carried out with the following conditions. The Al-Cr compositions (at. %) that were investigated are $x_{Cr} = 0, 0.1, 0.5, 0.75, 1$ and 7 respectively. Simulations were performed using the MEAM potential developed in this work and were compared with a model from the Finnis and Sinclair (FS) formalism⁶⁹.

4 Results and discussion

4.1 Effect of the reference structure on the modeling of liquid Zr

Current interatomic potential models for elements are typically developed from their known reference structure at standard conditions of temperature and pressure (i.e. 10^5 pascal and 298.15 K). At high temperatures and pressure, some elements undergo solid allotropic transformations. This is the case for metallic elements such as Zr, Ti, Fe, and Mn. The allotropic transformation from α (HCP)-Zr to β (BCC)-Zr takes place at 1135 K⁷², while its melting occurs at 2128.15 K⁷³. In perfect (i.e. defect-free) solid structures, the atomic motion is highly limited by the long-range ordering and symmetry of the crystal. In this case, vibration is the principal type of atomic motion. For real/macroscopic solids, defects such as vacancies, grain boundaries, and dislocations allow more degree of freedom to the atoms which become more mobile (diffusion is possible). For liquids, the long-range order and symmetry are broken. This allows the atoms to move more freely in this condensed phase. Short-range ordering is still preserved in liquids and is a direct function of the strength of the different interactions in the melt. Moreover, it is known that only a small coordination shell (up to second or third nearest neighbors) typically impacts the cohesive energy of metallic condensed phases^{74,75}. In this context, how is this short-range ordering affected by the selection of the solid reference structure used for EMD? In other words, we need to identify which reference structure is more suitable for the description of liquid phases. This question was addressed in our work by simulating liquid Zr using an HCP-referenced pairwise interatomic potential available in the literature²⁷ and a BCC-referenced potential developed in this work (Table 1). Liquid simulation cells of 500 atoms were equilibrated at 2000 K during 50 ps in the NPT ensemble using KISSMD.

Figure 4a shows the effect of the solid reference structure of Zr on the radial distribution function (RDF) of liquid Zr at 2000 K. The Zr-BCC potential shows a better agreement with the experimental data of Schenk et al⁷¹. Experimental data was derived from structure factor measurements by neutron diffraction, followed by a Fourier transformation⁷¹. This figure also shows that the Zr-HCP potential is less accurate when compared to the experimental data. In fact, the predicted radial distribution function curve with this reference structure was closer to the *Ab Initio* Molecular Dynamics data at 2000 K reported by Jakse & Pasturel⁷⁰. For the case of the Angular Distribution Function (ADF) (Figure 4b), both BCC-based (blue line) and HCP-based (red line) results are slightly shifted to higher angles when compared to *Ab Initio* Molecular Dynamics calculations at 2000 K (Diamond symbols) from Jakse & Pasturel⁷⁰. The BCC reference potential again outperforms the HCP reference potential. One explanation to justify why the BCC-based potential provides a much better agreement with the experimental data is that it is also the primary solidification structure upon the cooling of liquid Zr. The local ordering of this structure is also closer to the one experienced in the liquid. Moreover, the BCC structure is the stable Zr allotrope for a wide range of temperatures (i.e. from 1135 K to 2128.15 K). It

is clear from these simulations that the reference solid structure has a direct impact on the local ordering of the liquid since the cohesive energy is tuned based on the local atomic environment (2NN approximation). These results also imply that the determination of physical properties of molten alloys including Zr in classical MD need to be performed using the BCC reference potential to ensure high accuracy. For low-temperature simulations (ex.: when calculating the energetics of partially ordered solid solutions), it is preferable to use the HCP reference as the BCC reference would lead to erroneous enthalpies (the contribution of the BCC-HCP allotropic transformation would not be accounted for in the simulations).

4.2 Potential transferability when evaluating the enthalpy of mixing of binary liquid solutions

The next case study to judge the transferability of classical interatomic potentials was the evaluation of the enthalpy of mixing of binary liquid solutions. To do so, liquid simulation cells of 500 atoms were equilibrated at specific compositions and temperatures during 30 ps by simulation steps of 1 fs. Enthalpy of mixing of Al-Cu at 1500 K using AlCu₃-L1₂, AlCu-BCC, and Al₃Cu-L1₂ as reference structures are presented in Figure 5. Modeling with the AlCu₃-L1₂ reference (green line and dots) exhibited the best description when compared with both experimental data and classical thermodynamic calculations. This metastable reference structure is isotropic. This Al-Cu interatomic potential version also leads to good agreement with the enthalpy of formation curve of solids computed with classical thermodynamics as presented in the force field development section of this work (Figure 1). Moreover, the AlCu₃-based interatomic potential of this work was compared with a recent MEAM potential from Mahata et. al⁷⁶ (blue line and points in Figure 5) and with the Angular-Dependent interatomic Potential (ADP) proposed by Apostol & Mishin⁷⁷ (purple line and points in Figure 5). The MEAM potential developed in this work showed the best accuracy for describing the enthalpy of mixing for the Al-Cu system.

Enthalpy of mixing curves for Al-Cr, Al-Zr, and Zr-Ti liquid systems at 2000 K were computed using EMD (Figures 6, 7 and 2, respectively). The energetic description of the Al-Cr liquid phase using the MEAM potential of this work was in agreement with experimental data and thermodynamic calculations (Figure 6). On the other side, the FS potential drastically overestimated the strength of the Al-Cr interatomic interaction within the liquid phase. The authors have reported satisfactory description for specific FeCrAl ferrite-based alloys using this potential⁶⁹. However, it appears from our simulations that this Al-Cr potential is not transferable to the exploration of Al-Cr liquid solution structures. The description of the Al-Zr liquid was also in good agreement with the enthalpy of mixing experimental data of Witusiewicz et al.⁸² (Figure 7). Finally, the enthalpy of mixing for Ti-Zr the liquid solution evaluated with our MD simulations oscillated around zero, implying an ideal solution behavior which is consistent with the thermodynamic description of this liquid solution (Figure 2).

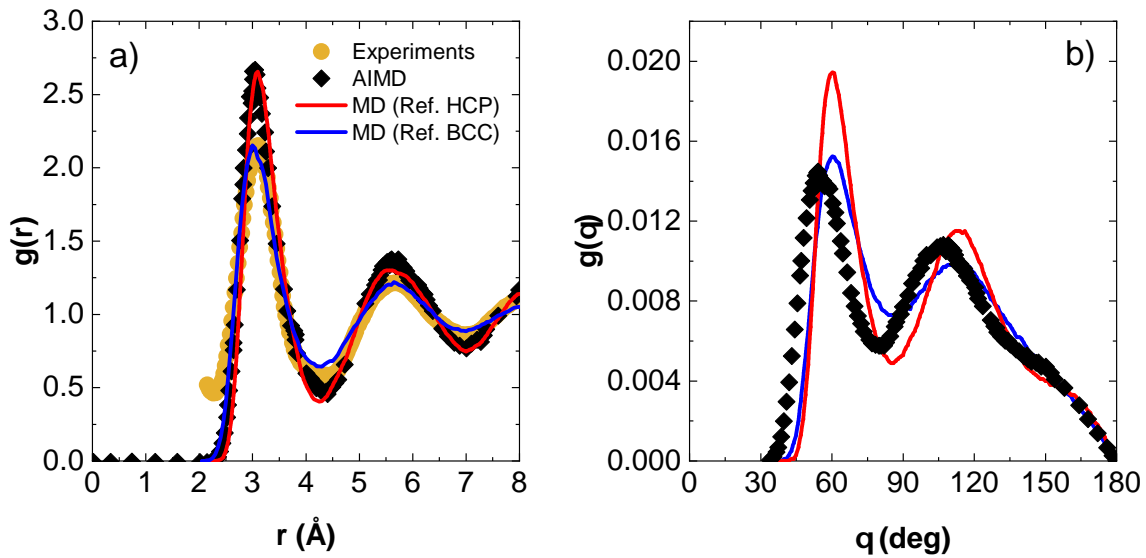


Fig. 4 (a) Total Radial Distribution Function (RDF) for liquid Zr at 2000 K computed with MD for BCC (blue line) as reference structure and HCP (red line) as reference structure using the MEAM formalism. Diamond symbols are results from *Ab Initio* Molecular Dynamics at 2000 K from Jakse & Pasturel⁷⁰. Dark yellow circles correspond to experimental data of Schenk et al⁷¹. The Angular Distribution Function (ADF) is presented in (b) for liquid Zr at 2000 K for BCC as reference structure (blue line) and HCP as reference structure (red line). Diamond symbols are results from *Ab Initio* Molecular Dynamics at 2000 K from Jakse & Pasturel⁷⁰.

4.3 Potential transferability for describing the internal structure of the Al₈₀Cu₂₀ melt

The internal structure of liquid solutions is another critical parameter when studying the nucleation of solids during solidification. Therefore, the selected classical interatomic potential needs to capture the short range ordering behavior of liquids if one wants to obtain useful insights from EMD. Al₈₀Cu₂₀ liquid simulation cells of 4 000 atoms were equilibrated at 1818 K during 0.5 ns by steps of 1 fs in the NPT ensemble. For the sake of comparison, EMD simulations were performed using the force field model based on the Al₃Cu-L1₂ reference developed in this work (table 2), the MEAM potential of Mahata et. al⁷⁶ and an Angular-Dependent interatomic Potential (ADP) from Apostol & Mishin⁷⁷. Radial Distribution Function (RDF) and Angular Distribution Function (ADF) were averaged and extracted for the last 100 000 steps for each simulation. Structural properties were compared to AIMD of Wang et al.⁸⁷. The total RDF computed by MD with these three different interatomic potentials present equivalent accuracy compared to AIMD (Figure 8a). The position of the first peak of the generalized RDF (Figure 8a) corresponds to the first nearest neighbor distance (r_{1NN})⁸⁸. Its length obtained from all the EMD simulations adequately matched the one obtained by AIMD. The first minimum of the RDF corresponds to the shell of first nearest neighbors (r_{1NN}^{shell})⁸⁹. This value is used as an integration limit to obtain the coordination number (Z) through $Z = \int_0^{r_{1NN}^{shell}} \rho_0 g(r) 4\pi r^2 dr$, where ρ_0 is the mean number density and $g(r)$ is total RDF (equation 10). Atomistic simulations performed using the ADP interatomic potential provided a closer value of r_{1NN}^{shell} compared to AIMD. Both MEAM potentials models provide a slight shifting of the r_{1NN}^{shell} toward higher values. The coordi-

nation number with the MEAM potential of Mahata et al. was higher than the one in the closest packed FCC and HCP solids. Coordination numbers with the MEAM potential of this work and the ADP model are lower than 12 but significantly higher than the AIMD prediction (i.e. 9.6). Wang et al.⁸⁷ reported that the coordination number of Al₈₀Cu₂₀ melts increased by decreasing temperature, up to 11 at 1000K. This behavior has also been experimentally observed in Al₆₀Cu₄₀ melts, with values of 11.26 and 11.50 at 1323K and 973K respectively⁹⁰. Important deviations are observed in the partial RDF for the Al-Cu pair (Figure 8b) for most MD simulations, MEAM potential developed in this work shows the best accuracy for describing the Al-Cu pair distribution compared to AIMD calculations.

4.4 Potential transferability for the energetic description of isotropic and anisotropic solids

4.4.1 Al-Cu system

Solidification processes imply that solid particles will start to nucleate as the temperature is lowered below a critical value. Interatomic potentials should also be able to adequately describe solid solutions. Modeling of solid compounds within the Al-Cu system has been compared with three interatomic potentials, the AlCu₃-L1₂ MEAM potential of this work, the MEAM potential of Mahata et al.⁷⁶ and the ADP from Apostol & Mishin⁷⁷ (Table 4). Note that numerical data obtained from the MEAM potential developed by Mahata et al.⁷⁶ were directly taken from their published article. Unfortunately, we were not able to reproduce these values in our MD simulations using their provided interatomic potential file. For the isotropic Cu-rich L1₂ compound, the MEAM potential provided a better description than the ADP when compared

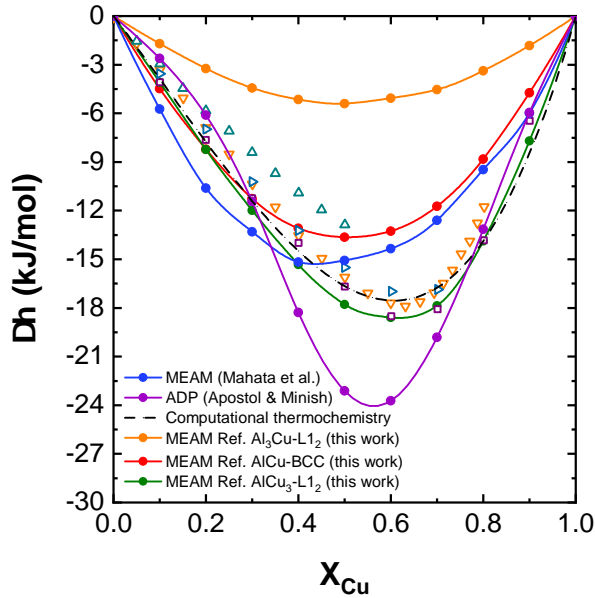


Fig. 5 Molar enthalpy of mixing for liquid Al-Cu. Filled circles and line are the thermodynamic data calculated with MD at $T=1500$ K. Experimental data from Stolz et al.⁷⁸ (orange triangles) at 1467 K, Kanibolotsky et al.⁷⁹ (blue triangles) at 1590 K, Gizenko et al.⁸⁰ (purple squares) at 1473 K, and Sandakov et al.⁸¹ (cyan triangles) at 1773 K are presented as open symbols. Dashed line are results at 1500 K from classical thermodynamics performed with FactSage⁵⁷.

to the DFT prediction. The opposite was observed for the Al-rich $L1_2$ structure. For the cubic AlCu-B2, both MEAM potentials overestimated the energetics of this phase, and the ADP showed the best accuracy. None of the three potentials is able to reproduce the entire set of phases, the predicting capability of EMD potentials is, therefore, dependent on the formalism employed during potential parametrization.

Table 4 Calculated enthalpy of formation (eV/atom) for Al-Cu metastable compounds. Results are compared to other MD models and first-principle calculations.

Formula	Structure	MEAM (this work)	MEAM ⁷⁶	ADP ⁷⁷	DFT
Al ₃ Cu	L1 ₂	-0.152	-0.180	0.100	-0.037 ⁵⁶
Al ₃ Cu ₂	D5 ₁₉	-0.182	-0.299	-0.342	-0.164 ⁹¹
AlCu	B2	-0.317	-0.435	-0.635	-0.139 ⁵⁶
AlCu	B1	0.421	-0.205	-0.079	...
AlCu	"40" (NbP)	0.150	-0.016	-0.117	-0.191 ⁹²
AlCu	B32	-0.191	-0.009	-0.085	0.024 ⁹²
Al ₄ Cu ₉	D8 ₃	-0.139	-0.136	-0.331	-0.215 ⁷⁷
AlCu ₃	L1 ₂	-0.143	-0.179	-0.162	-0.181 ⁵⁶
AlCu ₃	A15	-0.070	-0.141	-0.196	...
AlCu ₃	D0 ₂₂	-0.142	-0.185	-0.226	-0.185 ⁹³

4.4.2 Al-Cr system

Enthalpy of formation at 0 K of Al-Cr solid compounds using the MEAM potential developed in this work are compared to DFT calculations available in the literature in Table 5. Energetic description of compounds was also compared to MD predictions using the FS potential from Lui et al.⁶⁹. The MEAM potential was able

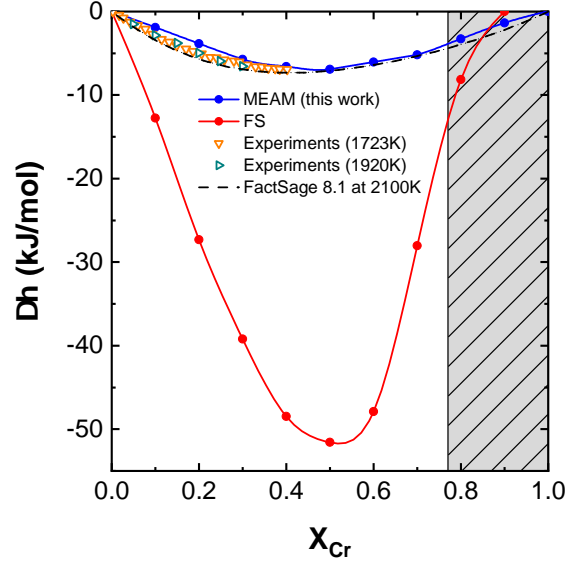


Fig. 6 Enthalpy of mixing at 2000K calculated with MD using the MEAM potential (filled blue circles and line) and the FS potential (filled red circles and line)⁶⁹. Experimental data from Saltykov et al.⁸³ (orange triangles) at 1723 and Sudavtsova et al.⁸⁴ (cyan triangles) at 1920 K are as open symbols. Dashed line are results at 2100 K from classical thermodynamics performed in FactSage⁵⁷. Shaded grey zone correspond to the meta-stability zone of the liquid at 2000K.

to provide a better energetic description of the AlCr₂ and Al₃Cr compounds. However, the crystal structure of Al₄₅Cr₇ and Al₈Cr₅ changed during the volume optimization (energy minimization) when using the MEAM formalism. FS potential considerably overestimates the formation energies of all solid compounds compared to DFT.

Table 5 Enthalpy of formation of different Al-Cr solid compounds at 0K compared with first-principle calculations and MD simulations. Formation energies are reported in eV/atom.

Formula	Space group	MEAM (this work)	FS ⁶⁹	DFT ⁵⁶
AlCr ₂	I4/mmm	-0.120	-0.634	-0.122
Al ₃ Cr	I4/mmm	-0.097	-0.534	-0.140
Al ₄₅ Cr ₇	C2/m	Crystal structure changes	-0.285	-0.117
Al ₈ Cr ₅	R3m	Crystal structure changes	-0.435	-0.054

4.4.3 Al-Zr-Ti system

Modeling of different Al-Zr-Ti solid compounds using the ternary MEAM interatomic potential of this work is presented in Table 6. Overall, this potential shows a good predicting capability for binary and ternary compounds of this ternary system.

4.5 MD simulations of the crystallization of pure aluminum

The next step after validating the transferability of the interatomic potentials developed in this work was to apply them for the description of solidification processes. We started with the exploration of the solidification of a pure element which theoretically occurs at a specific temperature for some imposed pressure. The

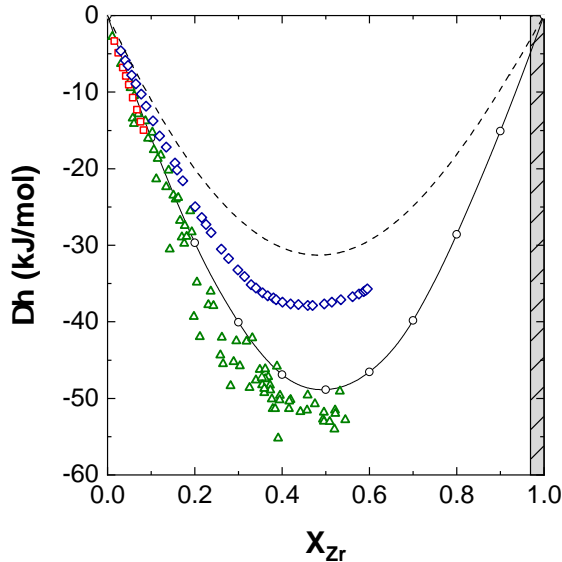


Fig. 7 Molar enthalpy of mixing for liquid Al-Zr. Open circles and line are the thermodynamic data calculated with MD at $T = 2000$ K. Experimental data from Esin et al.⁸⁵ (diamonds) at 1970 K, Sudavtsova et al.⁸⁶ (squares) at 1790 K, and Witusiewicz et al.⁸² (triangles) at 2080 K are presented as open symbols. Dashed line are results at 2000 K from classical thermodynamics performed in FactSage⁵⁷. The shaded grey zone corresponds to the meta-stability zone of the liquid at 2000K.

Table 6 Enthalpy of formation of different solid compounds within the Al-Zr-Ti system compared with first-principle calculations. Formation energies are reported in eV/atom.

Formula	Space group	MEAM (this work)	DFT ⁵⁶
TiAl	Pm3m	-0.260	-0.265
Al ₃ Ti	I4/mmm	-0.273	-0.398
ZrTi ₂	P6mmm	0.032	0.033
Zr ₃ Al	Pm3m	-0.296	-0.302
Al ₃ Zr	I4/mmm	-0.340	-0.487
Zr ₂ TiAl	Fm3m	-0.223	-0.160
ZrTi ₂ Al	Amm2	-0.333	-0.238

following thermal program was defined to melt, equilibrate and solidify the initially perfect Al-FCC supercell containing 200 000 atoms: equilibration into the NVT ensemble at 2.5 K for 0.5 ns, NPT heating at 1.66 K/s, NVT equilibration at 2000K during 0.5 ns followed by 0.5 ns of NPT modeling at the same temperature. Cooling was executed at -1K/ps. Finally, systems were equilibrated at 300K for 2ns. Crystallization results for pure aluminum are presented in Figure 9a. The evolution of the temperature as a function of the simulation time is represented by the red line for the MD simulations performed using the Finnis and Sinclair (FS) potential⁶⁹ while the blue line provides the results for the MEAM potential developed in this work. Screenshots of the simulation supercells showing only FCC-oriented atoms are presented for specific simulation steps. This provides a visual appreciation of the melting and solidification mechanisms during the programmed thermal treatment. Melting of the pure and perfectly ordered FCC aluminum supercell using the FS potential occurred at around 700 K, which is 233 K less than the experimental value.

Melting with the MEAM potential took place at around 1150 K. A higher melting temperature was expected because the initial configuration was a perfectly ordered FCC supercell without any defects. Since vacancies, dislocations, and grain boundaries are not considered, a higher amount of energy is required to overcome the perfect-lattice energy barrier for its mechanical melting. In other words, supplementary thermal energy is needed to induce the breaking of the long-range order symmetry of a crystal with no defects. Mechanical melting is related to elastic stability criteria for cubic systems, it occurs when the spinodal, shear or Born criteria are breached, i.e., $(C_{11} + 2C_{12} > 0)$, $(C_{44} > 0)$ and $(C_{11} - C_{12} > 0)$ respectively with C_{ij} being the elastic constant tensors⁹⁴. In MD, there exist several methods to properly predict the fusion temperature, such as the Pseudo-Supercritical Path (PSCP) approach, interface-based techniques, and the voids method⁹⁵. Even though the accurate melting description is out of the scope of this work, it can be observed that the FS potential is not suitable for this type of simulations since the melting point from a perfect FCC lattice is already lower than the experimental value.

The cooling process of the liquid system can be observed between 2.3 ns and 4 ns in Figure 9a. Simulation results show that undercooled liquid modeled with the MEAM potential was able to crystallize into the α -FCC at around 3.95 ns. A deviation from the perfect linear temperature profile which was programmed in the MD simulation is observed at around 4 ns. This temperature peak is associated with the release of latent energy caused by solidification. The degree of undercooling in this MD simulation is significantly higher than those observed experimentally (around 5-10 degrees according to the experiments of Guan et al.⁹⁷). Guan et al.⁹⁷ have reported that the undercooling, ΔT ($^{\circ}\text{C}$), increases by increasing the cooling rate. They reported ΔT ($^{\circ}\text{C}$) of 4.94, 7.18, 9.91 for cooling rates of 5, 10 and 20 K/min, respectively. Because of the extremely high quenching rates allowed in MD for large-scale simulations, it leads to high undercoolings compared to experimental observations. For the molten aluminum super-cell described by the FS-potential, an additional relaxation at 300 K after cooling (>4 ns) was needed in order to germinate the FCC-matrix. Simulations cells at 6 ns correspond to the final configurations of the systems at 300 K. Empty spaces stand for atoms with a local ordering different from the FCC. The final crystal obtained with the FS potential accounted for 32.4% of FCC-oriented atoms and 59.5% of HCP. Conversely, the MEAM potential exhibited a more coherent crystallization with 82% of FCC and only 14.9% of HCP. The coexistence of both the FCC and the metastable HCP phases is commonly found in MD simulations for aluminum⁴⁷. These structures actually share several characteristics: 1) they have the same atomic packing factor of 74%, they present similar interstitial sites, and 3) they both have 12 first nearest neighbors. Papanikolaou et al.⁹⁸ evaluated the effect of the cooling rate from 0.5 K/ps to 12 K/ps on the local structure of pure Al. They found the proportions of FCC and HCP are dependent on the cooling rates. FCC/HCP mixture is promoted at low cooling rates and this ordering is less favored as the cooling rate is increased. Here, the cooling rate was 1K/ps for both samples; hence, the proportion of HCP ordering upon solidification is rather related to the impact of the potential parametrization. A

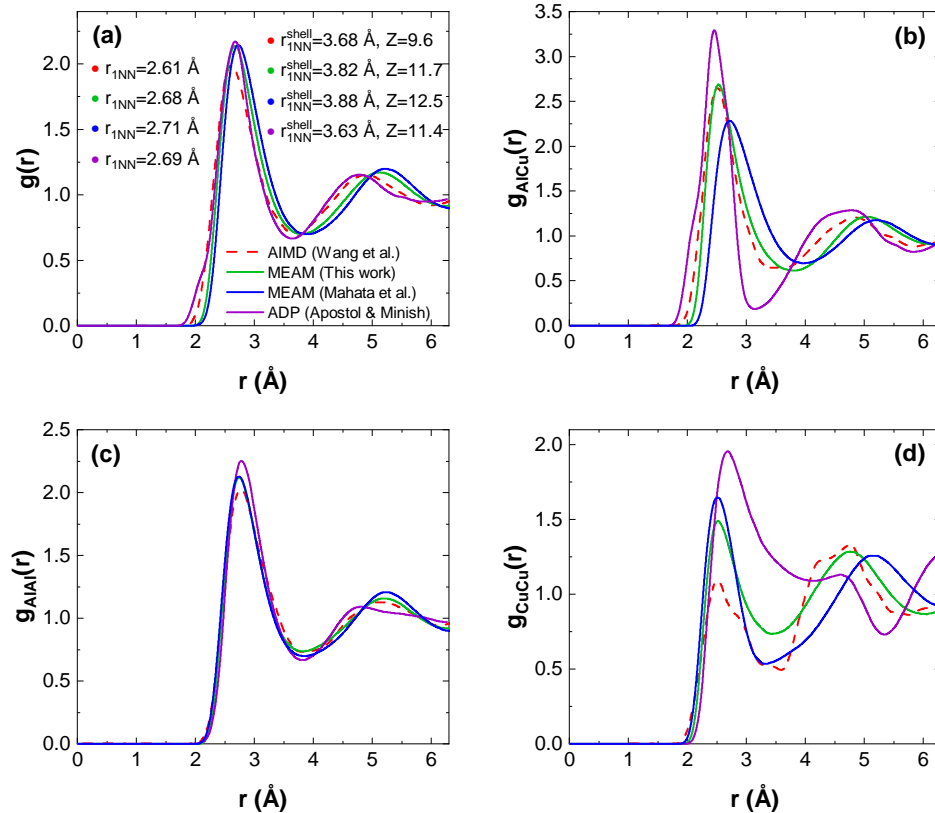


Fig. 8 Calculated total (a), and partial Al-Cu (b), Al-Al (c) and Cu-Cu (d) radial distribution functions for liquid $\text{Al}_{80}\text{Cu}_{20}$ at 1818 K. Results from different classical MD models are compared to AIMD data. The shell radius of first nearest neighbors (r_{1NN}^{shell}), the average first nearest neighbor distances (r_{1NN}), and the total coordination number (Z) are indicated.

detailed description of the local ordering during the simulations is presented in Figure 9b. Independently from the potential used in each simulation, there is a clear relationship between the icosahedral ordering (yellow lines in Figure 9b) and the FCC-oriented atoms (green lines) before and after crystallization. The icosahedral ordering consists of 12 atoms arranged around a central atom in the core of an icosahedron (Figure 10). It was proposed by Frank⁹⁹ to explain the energy minimization associated with local atomic arrangement during undercooling. As such, the maximum in the icosahedral fraction curve defines the maximum undercooling by icosahedral-related constraints. In other words, nuclei for FCC germination may start forming at this stage.

Figure 11 shows the graphical correlation between the icosahedral-oriented atoms (yellow) and FCC ordering (green) for the simulation of pure aluminum using the FS potential. Icosahedral orientation is rapidly rearranged into the FCC matrix of growing grains. By the end of solidification, only a minor icosahedral ordering of atoms is observed at the grain boundaries. Casada & Poon¹⁰⁰ reported that the icosahedral ordering was promoted at the grain boundaries of Al-Mg-Zn, Al-Mg-Cu, Al-Li-Zn, and Al-Li-Cu alloys during annealing. Minimum in the icosahedral ordering curve (Figure 9b) suggests the end of solidification.

4.6 Crystallization of model Al-Cr alloys by icosahedral-enhanced nucleation

The addition of alloying elements to a pure metallic system will have a direct impact on its melting and solidification behavior. This section considers the effect of Cr on the nucleation of model Al-Cr alloys. It also shows the impact of the interatomic potential on the solidification behavior of this system. A similar heat program to the one used for the pure aluminum study was implemented here as it can be seen in Figure 9a. The difference lies in the composition of the initial simulation supercells. Herein, Cr atoms were randomly distributed into the perfect-FCC lattice at different atomic concentrations of Cr (Figure S2). According to the Al-Cr equilibrium phase diagram calculated using the FTLite database of FactSage⁵⁷, which is presented in Figure S3, the α -matrix is the primary phase upon solidification of Al-Cr alloys up to 0.15 at.% of Cr. Above this composition, $\text{Al}_{13}\text{Cr}_2$ is the first intermetallic to precipitate up to 0.95 at.%. Lastly, $\text{Al}_{11}\text{Cr}_2$ is the primary phase for Al-Cr alloys containing 7 at.% of Cr.

Local chemical ordering results for the last MD configuration of each model binary Al-Cr alloys are displayed in Figure 12. The local ordering presented in this figure was evaluated with the Common-Neighbor Analysis (CNA) and Polyhedral Template Matching (PTM)⁶⁶ of OVITO⁹⁶. Firstly, it can be seen that the

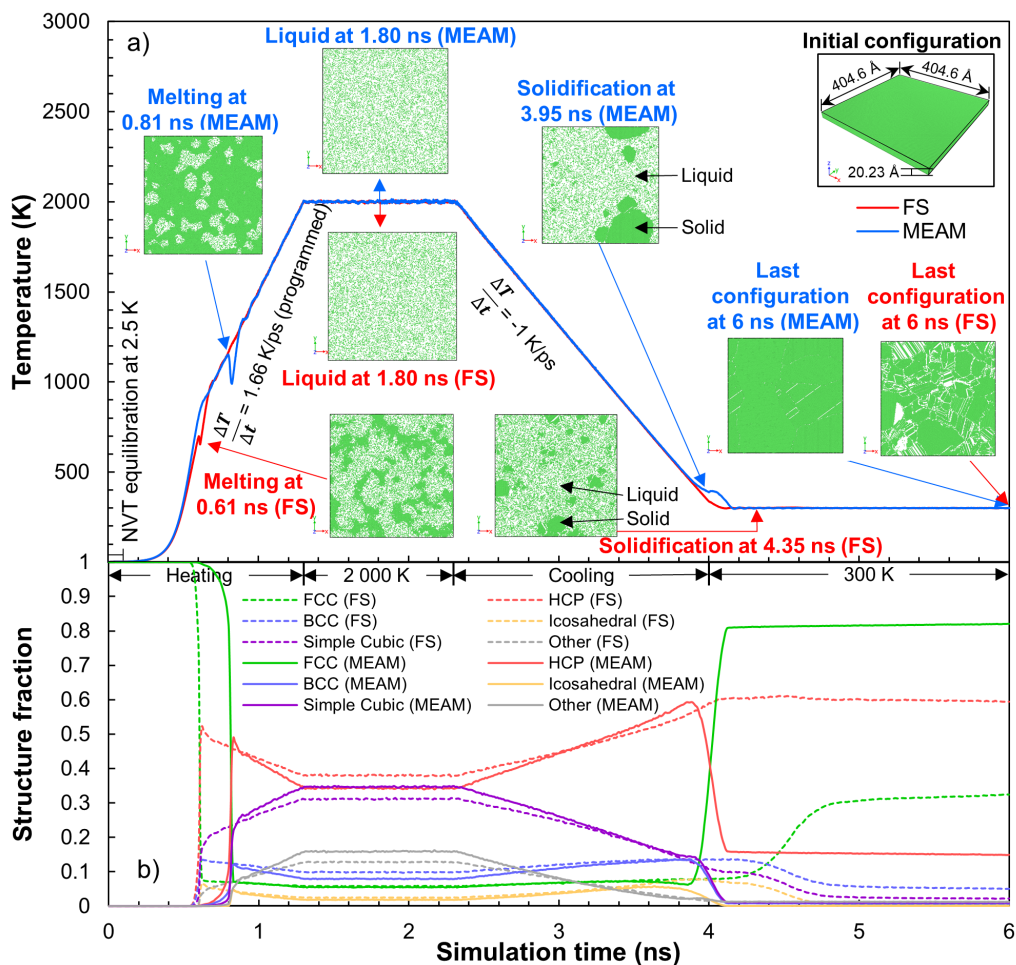


Fig. 9 (a) Scheme for time versus temperature during the classical MD simulation of melting/cooling of pure aluminum using the FS and MEAM potentials. Snapshots of simulated microstructures at specific simulation times are reported. Only FCC-oriented atoms are presented in the simulation boxes (green atoms). Systems were first equilibrated into the NVT ensemble at 2.5 K for 0.5 ns. NPT heating at 1.66 K/s was subsequently imposed. Then, NVT equilibration was carried at 2000K during 0.5 ns followed by 0.5 ns of NPT modeling at the same temperature. Cooling was executed at -1K/ps. Finally, systems were equilibrated at 300K. (b) Time-temperature evolution of the local ordering in solid/liquid aluminum, calculated via the Polyhedral Template Matching method^{66,96}. Calculated values with the MEAM potential (solid lines) in comparison with that obtained with the FS interatomic potential⁶⁹ (dashed lines).

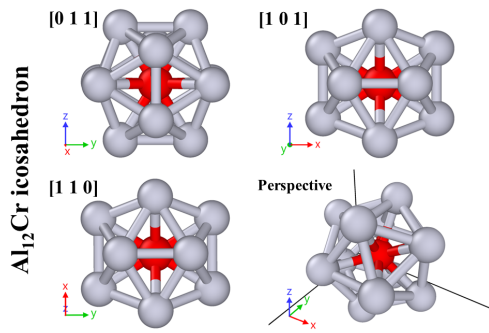


Fig. 10 Different perspectives of an Al_{12}Cr icosahedral cluster equilibrated at 0K (Al is in grey, Cr is in red).

MEAM potential outperforms the FS potential for all the compositions as it leads to a much more coherent solidification of nano α -FCC grains and minor HCP ordering due to twinning. The FS potential exhibits considerable fraction of HCP-oriented nano-zones in equilibrium with the FCC-phase for 0, 0.1, 0.5, 0.75, and 1 at.%. A metallic glass was obtained for 7at.% of Cr with the FS modeling. As anticipated by the nature of the atomic scale MD simulations, the primary intermetallics which should have formed as predicted from classical thermodynamics (Figure S3) were not able to nucleate. This is mainly caused by the high cooling rates which are typically imposed in MD simulations. As a result, the FCC was the primary phase during the solidification process of all our MD simulations using the MEAM potential, even with a high amount of Cr. This is a result of the out-of-equilibrium conditions imposed by the simulations and resulted in the supersaturation of the FCC phase. Strategies to overcome this problem when studying solidification include the interface method where a liquid supercell is coupled to a solid interface of the primary phase¹⁰¹. Aside from that, classical molecular dynamics performed in the NPT and NVT ensembles solely rely on enthalpy contributions to modulate the energetics and dynamics of the system. As such, entropy effects which play an important energetic role, especially at high temperatures, are not integrated. Apart from this important limitation, the preference of atoms in a liquid to cluster/aggregate and eventually precipitate to form a solid intermetallic nuclei is strongly dependent on the electronic structure of the individual atoms. Current interatomic potential formalisms for MD are based on simplifications of the effect of the electronic structure of individual atoms on the energetics of metallic systems. This also restricts the exploration of the precipitation of solid phases different from the FCC matrix in classical MD simulations.

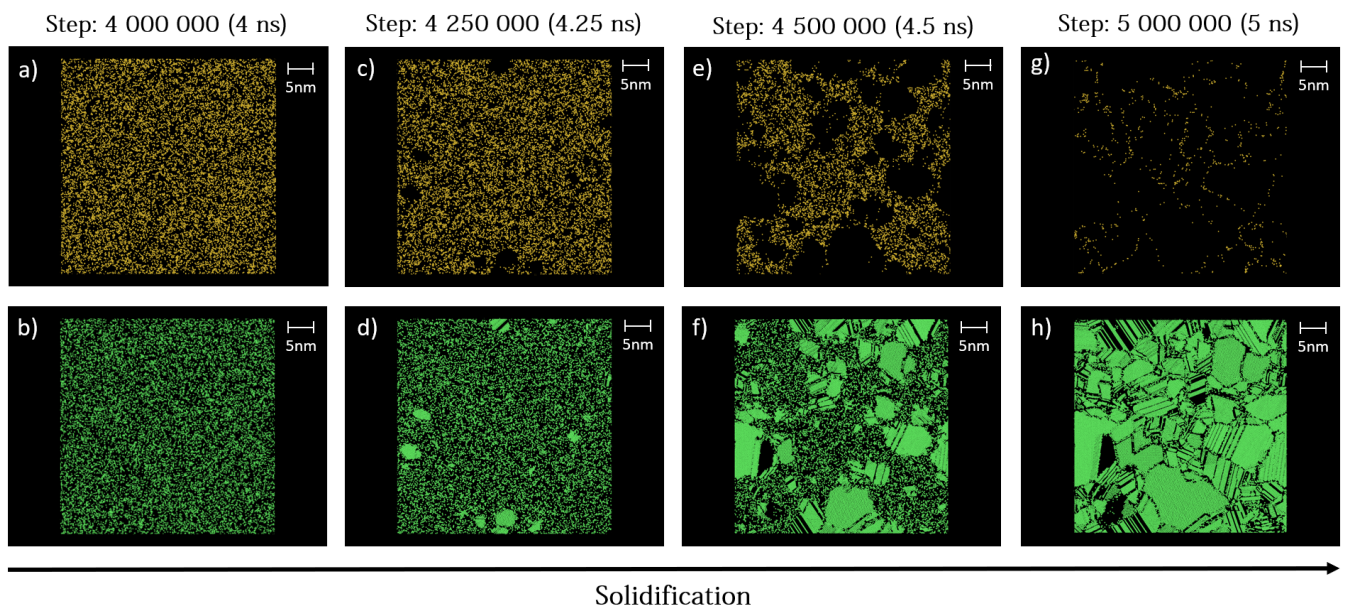


Fig. 11 Simulated partial local ordering via FS potential at specific simulation steps. Icosahedral-oriented atoms are presented in yellow and FCC in green.

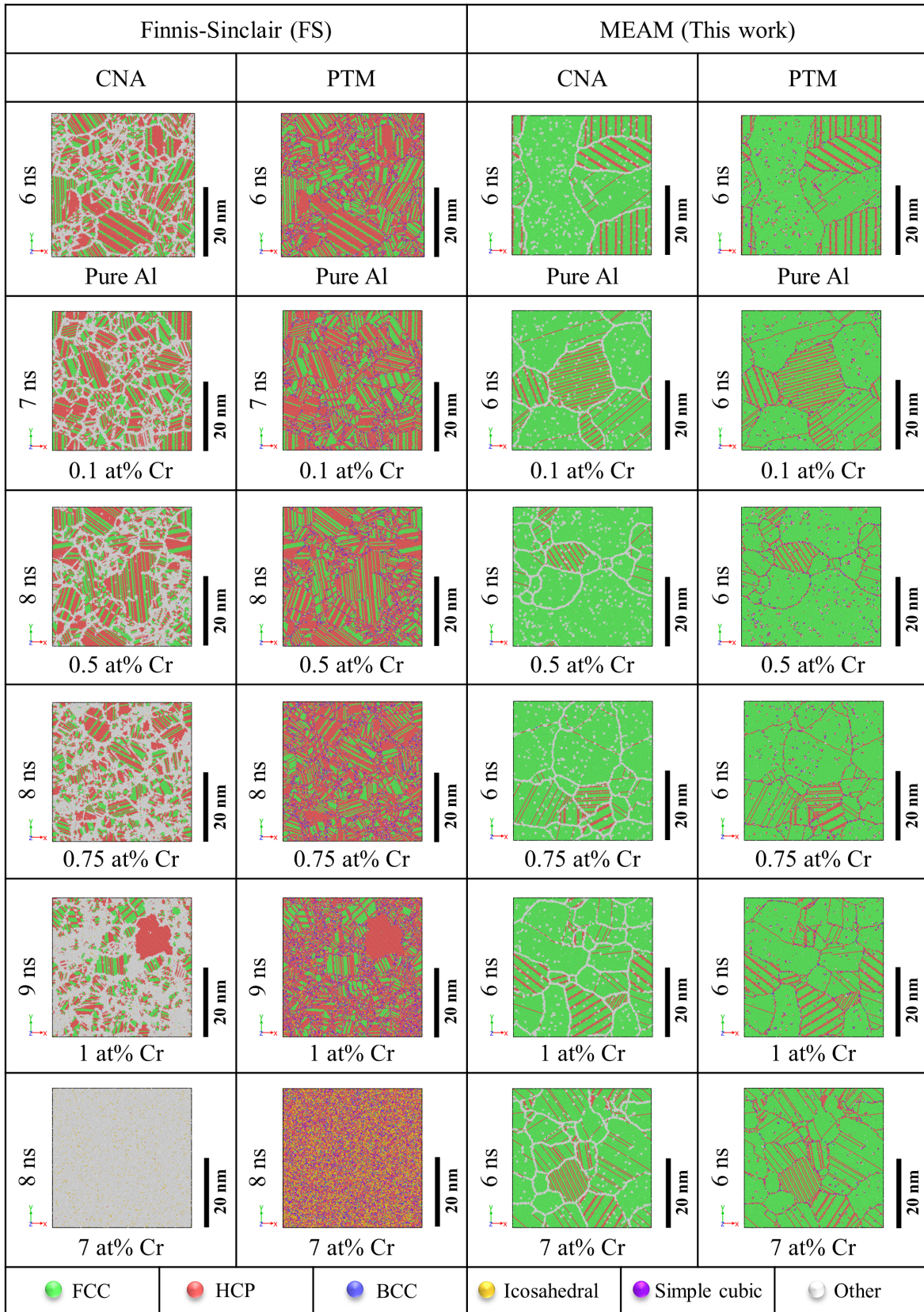


Fig. 12 Simulated microstructures for Al-Cr alloys at different compositions. The local ordering was determined via Common-Neighbor Analysis (CNA) and Polyhedral Template Matching (PTM).

Curves of temperature versus time for the different Al-Cr alloys using the MEAM potential are reported in Figure 13. Peaks at the end of the cooling curve correspond to the effect of the latent energy released from crystallization. Each stationary point in these curves indicates the effective nucleation of the FCC-phase, and thus, the beginning of latent energy release. The local maximum temperature after the stationary point shows an increase in the overall temperature of the supercell due to the phase transformation. These solidification peaks appear earlier in the solidification process as the amount of Cr in the alloy is increased. This implies that the addition of Cr into aluminum melts promotes the germination of the FCC phase with less undercooling when compared to pure aluminum. This is in agreement with the Icosahedral quasicrystal-enhanced nucleation theory for the germination of the FCC phase¹⁰². Kurtuldu et al.⁵² achieved grain refinement by this mechanism in an Al-Zn-Cr alloy with only 1000 ppm of Cr. The peaks at around 1 ns upon heating corresponds to the melting. More heating is needed as more Cr is present in the solid solution. This is a typical behavior of the peritectic Al-Cr system, in which the liquidus increases by increasing the amount of Cr in the alloy.

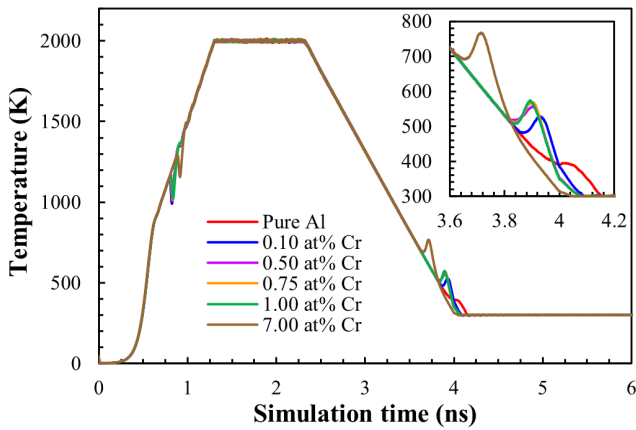


Fig. 13 Simulated temperature vs time for the different Al-Cr alloys. The inside figure shows the zoom of temperature perturbations during the cooling, which corresponds to the latent energy release of solidification.

The evolution of the icosahedral fraction during the MD simulations performed with the MEAM potential is presented at the top of Figure 14. The slope between the maximal (>3.5 ns) and minimal (<4.1 ns) values in the icosahedral ordering provides information about the kinetics of solidification. Pure Al had the least pronounced slope compared to Al-Cr alloys. This implies that solidification (nucleation + grain growth) took longer to be completed for this non-Cr-doped system. A steeper slope is obtained by increasing the amount of Cr in the Al-Cr alloys. This means that nuclei are more effective for the germination of the α -phase as more Cr is added into Al-Cr melts. The MD simulation with the highest amount of Cr (7%at.) solidified faster than the rest of the molten alloys. Note that this behavior is exclusive of the Al-Cr potential developed with the MEAM formalism; such as trend is not observed for the MD simulations performed with the FS potential (bottom of Figure 14). Instead, solidification

is slowed down when increasing the amount of Cr. Therefore, more time is required to achieve a critical amount of icosahedral fraction. Moreover, for the simulation supercell containing 7 at% of Cr, a metallic glass was obtained. This is a result of the largely overestimated strength of the Al-Cr interactions using the FS interatomic potential as presented in sections 4.2 and 4.4. All these results clearly show that the energetic description of these Al-Cr supercells with the Al-Cr FS interatomic potential provides a completely different solidification behavior to the MD simulations performed with the MEAM potential. The use of the MEAM potential led to a consistent description of the solidification where the icosahedral-enhanced germination of the FCC phase in Al-Cr melts occurs⁵². Therefore, an accurate description of the Al-Cr interatomic distance along with the prediction of its precise energetic strength are key ingredients to ensure a good transferability of the potential to describe complex phase transition phenomena such as bulk crystallization.

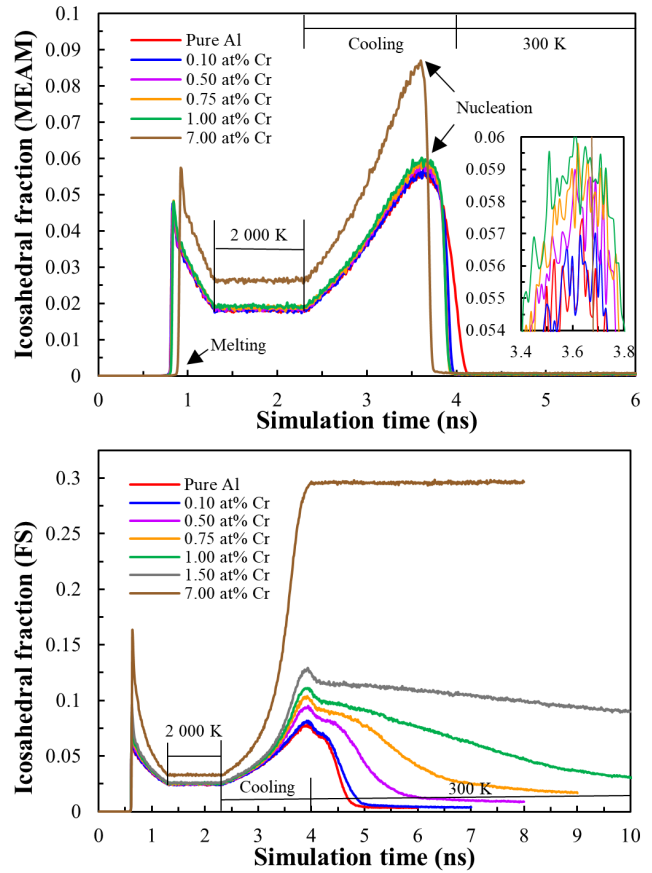


Fig. 14 Evolution of the icosahedral fraction over simulation time for different Al-Cr alloys using the MEAM (top) and FS (bottom) potentials.

Figure 15 shows the maximal icosahedral fraction achieved by all the Al-Cr melts prior to solidification for the simulations performed with the Al-Cr MEAM potential. Each value is related to the undercooling caused by icosahedral-related constraints. Pure Al reached a higher undercooling compared to all the other Al-Cr melts. This figure shows that the binary liquid solution with the highest concentration of Cr (7 at.%) exhibited the lowest undercooling. These values are higher than the stationary points

presented in the cooling curves (Figure 15) for all the compositions. In this case, an extra undercooling is required so that nuclei become effective for the precipitation of the FCC-phase. Figure 15 also shows that more icosahedral clusters are formed by increasing the amount of Cr in the melt. This confirms that the hypothesis of Kurtuldu et al.⁵² associating Cr with the formation of the ISRO was correct.

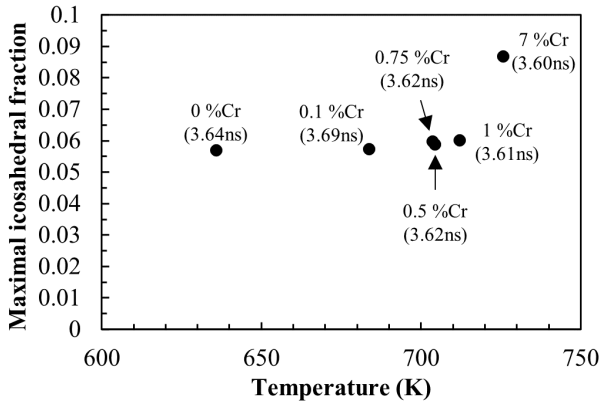


Fig. 15 Maximum icosahedral-related undercooling in Al-Cr alloys.

Figure 16 shows the overall time from the formation of the first nuclei (red points) to the end of solidification (black points). Pure aluminum displayed the longest time with 0.48 ns and the fastest solidification took place for the binary melt containing 7 at.% of Cr ($\Delta t = 0.16$ ns). While the time from effective germination of the FCC-phase (blue points) to the end of solidification (black points) is more or less equivalent for all the melts, the time for effective germination of the α -phase (from red to blue points) considerably changes from one composition to another. Nuclei in Al-7.at%Cr were more efficient for germination. More time for effective germination was needed as less Cr was present in the Al-Cr melts. Nucleation sites in pure Al were the least powerful resulting in a higher solidification time.

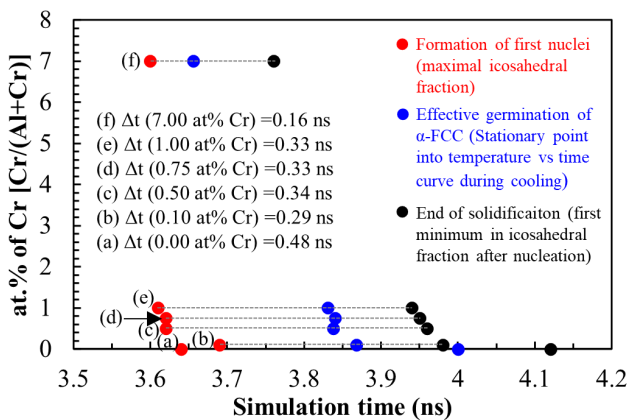


Fig. 16 Solidification stages correlated with the icosahedral ordering and the stationary point in the cooling curves of Al-Cr alloys.

Total energy vs temperature for all the simulations performed with the MEAM potential is presented in Figure 17. For all the

compositions, phase transformation was not isothermal. This deviation implies that energy release from solidification caused an increase in the temperature of the solid phase. The coexistence of solid and liquid phases occurred at lower temperatures for pure Al, because of the sued undercooling for effective nucleation when compared to Al-Cr melts.

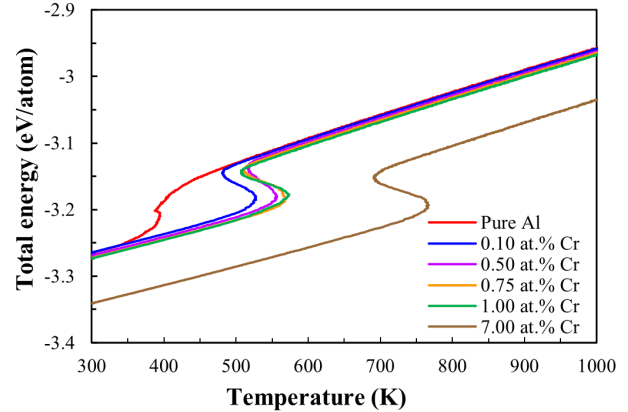


Fig. 17 Total energy versus temperature of for the different Al-Cr simulations.

Lastly, a grain analysis for the last configuration (at 6 ns) of all MD simulation cells modeled with the MEAM potential (Figure 18) was computed using the grain segmentation algorithm reported by Vimal et al.¹⁰³. Grain segmentation is compared to the Polyhedral Template Matching (PTM) results (shaded section in Figure 18). Explicitly, grain segmentation did not account for the twinning of coherent phases along the same grain. For this reason, a fourth column was added and corresponds to the twinning correction of coherent phases (FCC/HCP) belonging to the same grain. These were misleadingly identified as different grains by the grain segmentation algorithm. The third column of Figure 18 shows the number of grains as [corrected value accounting for twinning]/ [Total from grain segmentation algorithm]. Pure Al exhibited a smaller number of grains (4). Grain refinement was achieved for Al-Cr melts when compared to pure Al. Modeling of Al-Cr melts using the MEAM potentials was in agreement with the icosahedral-enhanced nucleation theory promoted by Cr, as experimentally reported by Kurtuldu et al.⁵².

It is to be pointed out that all these equiaxed-like simulated nanostructures were obtained from extremely fast cooling rates. In industrial applications, solidification cooling rates are orders of magnitude smaller (even during powder atomization from melts or laser additive manufacturing) and would result in either dendritic or cellular structures at a much larger scale (typically the micron scale). Moreover, the heat extraction in our MD simulations was non-directional (pseudo-isothermal cooling) which is never the case in real applications. At best, such pseudo-isothermal cooling would apply locally. Nevertheless, these nanostructures are highly reminiscent of typical microstructures obtained from slowly solidified alloys. Higher cooling power is involved in our MD simulations compared to the one obtained in real solidification processes. In our simulations, we remove about $[1.4 \times 10^7 \text{ W}/(\text{m}^2\text{K}) - 3.31 \times 10^7 \text{ W}/(\text{m}^2\text{K})]$, which is signifi-

cantly higher than the [370 W/(m²K) - 1917 W/(m²K)] interval in casting processes¹⁰⁴. Equivalently, we can view this in terms of the number of atoms that are ordered per second upon solidification which is much greater in MD simulations than in real-life applications. Further investigations are needed to determine the influence of these scaling factors from atomistic simulations to real-life conditions to understand how to transpose MD simulation results obtained with periodic boundary conditions to a larger scale.

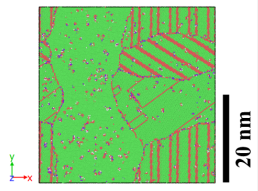
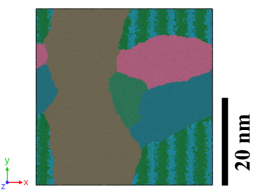

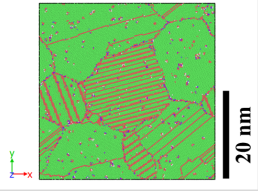
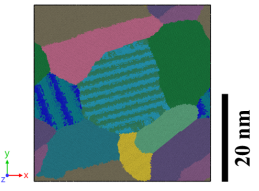
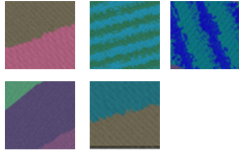
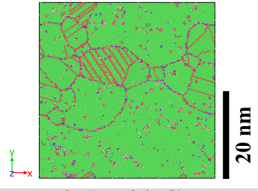
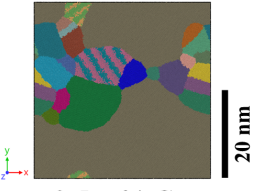
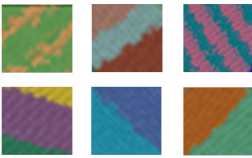
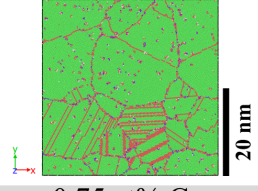
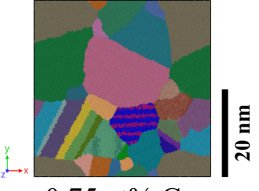
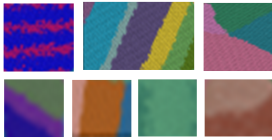
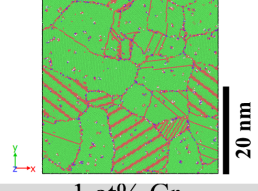
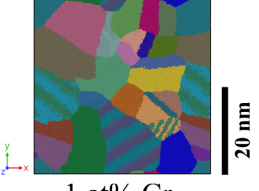
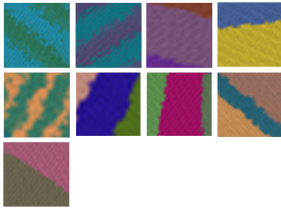
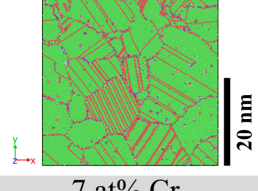
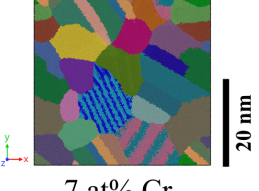
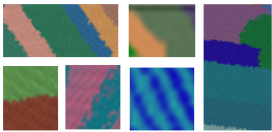






MEAM					
PTM	Grain segmentation	Estimated grains	Twinning correction		
 Pure Al	 Pure Al	4/6 Pure Al	 Pure Al		
 0.1 at% Cr	 0.1 at% Cr	6/12 0.1 at% Cr	 0.1 at% Cr		
 0.5 at% Cr	 0.5 at% Cr	16/24 0.5 at% Cr	 0.5 at% Cr		
 0.75 at% Cr	 0.75 at% Cr	15/31 0.75 at% Cr	 0.75 at% Cr		
 1 at% Cr	 1 at% Cr	17/30 1 at% Cr	 1 at% Cr		
 7 at% Cr	 7 at% Cr	14/31 7 at% Cr	 7 at% Cr		
 FCC	 HCP	 BCC	 Icosahedral	 Simple cubic	 Other

Fig. 18 Analysis of the local ordering via PTM analysis (first column) compared to the grain segmentation analysis for different Al-Cr alloys.

5 Conclusions

To investigate the transferability of the classical pairwise additive atomistic force field to the description of unary and multi-component systems, nano/mesoscale MD simulations were performed. It has been found that current interatomic potentials for Equilibrium Molecular dynamics (EMD) simulations are not entirely transferable to the description of complex systems. This is mainly due to the structure dependence of their parameterization. For unary and binary systems, interatomic models for EMD calculations have a reasonable predicting capability. However, simultaneous descriptions of anisotropic solids and the liquid phase can not be achieved for the entire range of compositions. This is why current interatomic potential remains limited for specific applications. The universality of interatomic potentials and the simplification of interatomic potentials based on pairwise contributions, along with the short length and time scales used in MD, are dominant aspects that limit the proper modeling of multi-component systems. This work opens up the way for developing more extensive interatomic potential formalisms.

The effect of the reference structure (BCC and HCP) on the modeling of pure liquid Zr has been assessed using the MEAM formalism. The BCC-based potential provided better agreement with the experimental as BCC is the stable phase at high temperature for this element. The importance of relying on classical thermodynamics during the parameterization of Al-Cu potentials was highlighted. The interatomic potential based on the AlCu₃-Li₂ metastable phase had the closest value of sublimation energy when compared to the solid enthalpy of formation curve of the Al-Cu system obtained by classical thermochemical calculations. This potential accomplished the best modeling of Al-Cu liquid compared to other models. Performance of the Finnis & Sinclair (FS) and the Modified Embedded-Atom Method (MEAM) interatomic potential formalisms has been compared during the crystallization of Pure Al and model Al-Cr alloys. While the MEAM formalism provides coherent solidification of the α -FCC matrix, the FS inadvisedly promotes a significant solidification of the HCP phase in equilibrium with the α -FCC matrix. The effect of Cr in Al melts was in agreement with the icosahedral nucleation of the α -Al phase by using the MEAM-based interatomic potential.

Acknowledgements

This research was supported by funds from the Natural Sciences and Engineering Research Council of Canada (NSERC), Alcoa, Hydro Aluminum, Constellium, Rio Tinto Aluminum, Elysis and the CRITM. This research was enabled in part by support provided by Calcul-Québec (www.calculquebec.ca) and Compute Canada (www.computeCanada.ca).

References

- 1 B. Zhou, B. Liu and S. Zhang, *Metals*, 2021, **11**, 718.
- 2 B. MacDonald, Z. Fu, B. Zheng, W. Chen, Y. Lin, F. Chen, L. Zhang, J. Ivanisenko, Y. Zhou, H. Hahn *et al.*, *Jom*, 2017, **69**, 2024–2031.
- 3 S. Imtiaz, I. S. Amiin, Y. Xu, T. Kennedy, C. Blackman and K. M. Ryan, *Materials Today*, 2021, **48**, 241–269.
- 4 J. L. Cann, A. De Luca, D. C. Dunand, D. Dye, D. B. Miracle, H. S. Oh, E. A. Olivetti, T. M. Pollock, W. J. Poole, R. Yang *et al.*, *Progress in Materials Science*, 2021, **117**, 100722.
- 5 I. Choudhury and M. El-Baradie, *Journal of Materials Processing Technology*, 1998, **77**, 278–284.
- 6 H. Long, S. Mao, Y. Liu, Z. Zhang and X. Han, *Journal of Alloys and Compounds*, 2018, **743**, 203–220.
- 7 R. Darolia, *International materials reviews*, 2019, **64**, 355–380.
- 8 M.-H. Tsai and J.-W. Yeh, *Materials Research Letters*, 2014, **2**, 107–123.
- 9 M. C. Gao, C. Zhang, P. Gao, F. Zhang, L. Ouyang, M. Widom and J. A. Hawk, *Current Opinion in Solid State and Materials Science*, 2017, **21**, 238–251.
- 10 L.-Y. Tian, G. Wang, J. S. Harris, D. L. Irving, J. Zhao and L. Vitos, *Materials & Design*, 2017, **114**, 243–252.
- 11 J. Allison, D. Backman and L. Christodoulou, *Jom*, 2006, **58**, 25–27.
- 12 J.-W. Yeh, *Jom*, 2013, **65**, 1759–1771.
- 13 J. Neugebauer and T. Hickel, *Wiley Interdisciplinary Reviews: Computational Molecular Science*, 2013, **3**, 438–448.
- 14 C. J. Cramer and D. G. Truhlar, *Physical Chemistry Chemical Physics*, 2009, **11**, 10757–10816.
- 15 D. Dickel, S. Mun, M. Baskes, S. Gwaltney, R. K. Prabhu and M. F. Horstemeyer, *Multiscale Biomechanical Modeling of the Brain*, Elsevier, 2022, pp. 39–52.
- 16 J.-P. Harvey, A. Gheribi and P. Chartrand, *The Journal of chemical physics*, 2011, **135**, 084502.
- 17 J.-P. Harvey, A. Gheribi and P. Chartrand, *Physical Review B*, 2012, **86**, 224202.
- 18 J.-P. Harvey, A. E. Gheribi and P. Chartrand, *Journal of Applied Physics*, 2012, **112**, 073508.
- 19 Y. Huang, J. Kang, W. A. Goddard III and L.-W. Wang, *Physical Review B*, 2019, **99**, 064103.
- 20 M. S. Daw and M. I. Baskes, *Physical Review B*, 1984, **29**, 6443.
- 21 M. Finnis and J. Sinclair, *Philosophical Magazine A*, 1984, **50**, 45–55.
- 22 F. Cleri and V. Rosato, *Physical Review B*, 1993, **48**, 22.
- 23 M. I. Baskes, *Physical review B*, 1992, **46**, 2727.
- 24 B.-J. Lee and M. Baskes, *Physical Review B*, 2000, **62**, 8564.
- 25 B.-J. Lee, M. Baskes, H. Kim and Y. K. Cho, *Physical Review B*, 2001, **64**, 184102.
- 26 B.-J. Lee, J.-H. Shim and M. Baskes, *Physical Review B*, 2003, **68**, 144112.
- 27 Y.-M. Kim, B.-J. Lee and M. Baskes, *Physical Review B*, 2006, **74**, 014101.
- 28 E. C. Do, Y.-H. Shin and B.-J. Lee, *Calphad*, 2008, **32**, 82–88.
- 29 Y.-M. Kim, N. J. Kim and B.-J. Lee, *Calphad*, 2009, **33**, 650–657.
- 30 H.-S. Jang, K.-M. Kim and B.-J. Lee, *Calphad*, 2018, **60**, 200–207.
- 31 S.-H. Oh, X.-G. Lu, Q. Chen and B.-J. Lee, *Calphad*, 2021, **75**, 102342.

- 32 Y.-K. Kim, W.-S. Jung and B.-J. Lee, *Modelling and Simulation in Materials Science and Engineering*, 2015, **23**, 055004.
- 33 Y.-K. Kim, H.-K. Kim, W.-S. Jung and B.-J. Lee, *Computational Materials Science*, 2017, **139**, 225–233.
- 34 H.-S. Jang, D. Seol and B.-J. Lee, *Journal of Magnesium and Alloys*, 2021, **9**, 317–335.
- 35 B.-J. Lee, W.-S. Ko, H.-K. Kim and E.-H. Kim, *Calphad*, 2010, **34**, 510–522.
- 36 S. Roy, A. Dutta and N. Chakraborti, *Computational Materials Science*, 2021, **190**, 110258.
- 37 S. Hu, M. Baskes, M. Stan and L. Chen, *Acta materialia*, 2006, **54**, 4699–4707.
- 38 B. Jelinek, S. Groh, M. F. Horstemeyer, J. Houze, S.-G. Kim, G. J. Wagner, A. Moitra and M. I. Baskes, *Physical Review B*, 2012, **85**, 245102.
- 39 S. Schönecker, X. Li, K. Koepf, B. Johansson, L. Vitos and M. Richter, *RSC advances*, 2015, **5**, 69680–69689.
- 40 M. Jin, N. Miao, W. Zhao, J. Zhou, Q. Du and Z. Sun, *Computational Materials Science*, 2018, **148**, 27–37.
- 41 J. Hafner, *Journal of computational chemistry*, 2008, **29**, 2044–2078.
- 42 S. Riniker, *Journal of chemical information and modeling*, 2018, **58**, 565–578.
- 43 E. Lee and B.-J. Lee, *Journal of Physics: Condensed Matter*, 2010, **22**, 175702.
- 44 P. Chartrand and A. D. Pelton, *Metallurgical and Materials Transactions A*, 2001, **32**, 1385–1396.
- 45 A. Dogan and H. Arslan, *Metallurgical and Materials Transactions A*, 2015, **46**, 3753–3760.
- 46 P. Srinivasan, L. Nicola and A. Simone, *Computational Materials Science*, 2017, **134**, 145–152.
- 47 Z. Hou, K. Dong, Z. Tian, R. Liu, Z. Wang and J. Wang, *Physical Chemistry Chemical Physics*, 2016, **18**, 17461–17469.
- 48 M. Mendeleev, M. Kramer, C. A. Becker and M. Asta, *Philosophical Magazine*, 2008, **88**, 1723–1750.
- 49 Q. Zhang, J. Wang, S. Tang, Y. Wang, J. Li, W. Zhou and Z. Wang, *Physical Chemistry Chemical Physics*, 2019, **21**, 4122–4135.
- 50 M. Mendeleev, S. Han, D. Srolovitz, G. Ackland, D. Sun and M. Asta, *Philosophical magazine*, 2003, **83**, 3977–3994.
- 51 J.-P. Harvey and P. D. Asimow, *American Mineralogist*, 2015, **100**, 1866–1882.
- 52 G. Kurtuldu, P. Jarry and M. Rappaz, *Acta Materialia*, 2013, **61**, 7098–7108.
- 53 S. Plimpton, *Fast parallel algorithms for short-range molecular dynamics*, Sandia national labs., albuquerque, nm (united states) technical report, 1993.
- 54 J. M. D. Lane, A. P. Thompson and T. J. Vogler, *Physical Review B*, 2014, **90**, 134311.
- 55 J. H. Rose, J. R. Smith, F. Guinea and J. Ferrante, *Physical Review B*, 1984, **29**, 2963.
- 56 A. Jain, S. P. Ong, G. Hautier, W. Chen, W. D. Richards, S. Dacek, S. Cholia, D. Gunter, D. Skinner, G. Ceder et al., *APL materials*, 2013, **1**, 011002.
- 57 C. W. Bale, P. Chartrand, S. Degterov, G. Eriksson, K. Hack, R. B. Mahfoud, J. Melançon, A. Pelton and S. Petersen, *Calphad*, 2002, **26**, 189–228.
- 58 Y.-K. Kim, H.-K. Kim, W.-S. Jung and B.-J. Lee, *Computational materials science*, 2016, **119**, 1–8.
- 59 S. Nosé, *The Journal of chemical physics*, 1984, **81**, 511–519.
- 60 W. G. Hoover, *Physical review A*, 1985, **31**, 1695.
- 61 S. Nosé, *Molecular physics*, 1984, **52**, 255–268.
- 62 W. G. Hoover, *Physical Review A*, 1986, **34**, 2499.
- 63 D. Frenkel and B. Smit, *Understanding molecular simulation: from algorithms to applications*, Elsevier, 2001, vol. 1.
- 64 A. Stukowski, *Modelling and Simulation in Materials Science and Engineering*, 2009, **18**, 015012.
- 65 D. Faken and H. Jónsson, *Computational Materials Science*, 1994, **2**, 279–286.
- 66 P. M. Larsen, S. Schmidt and J. Schiøtz, *Modelling and Simulation in Materials Science and Engineering*, 2016, **24**, 055007.
- 67 S. V. Sukhomlinov and M. H. Müser, *The Journal of chemical physics*, 2017, **146**, 024506.
- 68 J. Hafner, *Le Journal de Physique Colloques*, 1985, **46**, C9–69.
- 69 Z. Liu, Q. Han, Y. Guo, J. Lang, D. Shi, Y. Zhang, Q. Huang, H. Deng, F. Gao, B. Sun et al., *Journal of Alloys and Compounds*, 2019, **780**, 881–887.
- 70 N. Jakse and A. Pasturel, *Physical review letters*, 2003, **91**, 195501.
- 71 T. Schenk, D. Holland-Moritz, V. Simonet, R. Bellissent and D. Herlach, *Physical review letters*, 2002, **89**, 075507.
- 72 S. Banerjee, *Encyclopedia of Materials: Science and Technology*, Elsevier, Oxford, 2001, pp. 6287–6299.
- 73 D. Deardorff and E. T. Hayes, *JOM*, 1956, **8**, 509–510.
- 74 S. Chantasiriwan and F. Milstein, *Physical Review B*, 1996, **53**, 14080.
- 75 S.-H. Yoo, J.-H. Lee, Y.-K. Jung and A. Soon, *Physical Review B*, 2016, **93**, 035434.
- 76 A. Mahata, T. Mukhopadhyay and M. A. Zaeem, *Computational Materials Science*, 2022, **201**, 110902.
- 77 F. Apostol and Y. Mishin, *Physical Review B*, 2011, **83**, 054116.
- 78 U. Stolz, I. Arpshofen, F. Sommer and B. Predel, *Journal of phase equilibria*, 1993, **14**, 473–478.
- 79 D. Kanibolotsky, O. Bieloborodova, N. Kotova and V. Lisnyak, *Journal of thermal analysis and calorimetry*, 2002, **70**, 975–983.
- 80 I. Gizenko, S. Killeso, B. Yemlin and A. Zavyalov, *Izv. V. U. Z. Tsvetn. Metall.*, 1983, 39–41.
- 81 V. Sandakov, Y. O. Esin, P. Gel'd and V. Shantarin, *Zhurnal Fizicheskoi Khimii*, 1971, **45**, 2030–2032.
- 82 V. Witusiewicz, U. K. Stolz, I. Arpshofen and F. Sommer, *Zeitschrift fuer Metallkunde*, 1998, **89**, 704–713.
- 83 P. Saltykov, V. Witusiewicz, I. Arpshofen, H. Seifert and F. Aldinger, *Journal of Materials Science & Technology*, 2002, **18**, 167–170.

- 84 V. Sudavtsova, N. Sharkina and A. Shuvalov, *Rasplavy*, 1990, **1**, 97–99.
- 85 Y. O. Esin, N. Bobrov, M. Petrushevskij and P. Gel'd, *Izvestiya Akademii Nauk SSSR, Metally*, 1974, 104–109.
- 86 V. Sudavtsova, G. Batalin and V. Tutevich, *Russ. Metall.*, 1985, 183–185.
- 87 W. Wang, J. Han, H. Fang, J. Wang, Y. Liang, S. Shang, Y. Wang, X. Liu, L. Kecskes, S. Mathaudhu *et al.*, *Acta Materialia*, 2015, **97**, 75–85.
- 88 J. Ding, E. Ma, M. Asta and R. O. Ritchie, *Scientific reports*, 2015, **5**, 1–9.
- 89 J. A. van Meel, L. Filion, C. Valeriani and D. Frenkel, *The Journal of chemical physics*, 2012, **136**, 234107.
- 90 S. Wang, M. Kramer, M. Xu, S. Wu, S. Hao, D. Sordelet, K. Ho and C. Wang, *Physical Review B*, 2009, **79**, 144205.
- 91 W. Zhou, L. Liu, B. Li, Q. Song and P. Wu, *Journal of electronic materials*, 2009, **38**, 356–364.
- 92 D. Nguyen-Manh and D. Pettifor, *Intermetallics*, 1999, **7**, 1095–1106.
- 93 M. Mihalkovic and M. Widom, URL <http://alloy.phys.cmu.edu>, 2017.
- 94 B. Karki, G. Ackland and J. Crain, *Journal of Physics: Condensed Matter*, 1997, **9**, 8579.
- 95 Y. Zhang and E. J. Maginn, *The Journal of chemical physics*, 2012, **136**, 144116.
- 96 A. Stukowski, *Modelling and simulation in materials science and engineering*, 2009, **18**, 015012.
- 97 W.-B. Guan, Y.-L. Gao, Q.-J. Zhai and K.-D. Xu, *Materials Letters*, 2005, **59**, 1701–1704.
- 98 M. Papanikolaou, K. Salonitis, M. Jolly and M. Frank, *Metals*, 2019, **9**, 1217.
- 99 F. C. Frank, *Proceedings of the Royal Society of London. Series A. Mathematical and Physical Sciences*, 1952, **215**, 43–46.
- 100 W. Cassada, G. Shiflet and S. Poon, *Journal of Microscopy*, 1987, **146**, 323–335.
- 101 T. Fujinaga, Y. Watanabe and Y. Shibuta, *Computational Materials Science*, 2020, **182**, 109763.
- 102 M. Rappaz, P. Jarry, G. Kurtuldu and J. Zollinger, *Metallurgical and Materials Transactions A*, 2020, **51**, 2651–2664.
- 103 M. Vimal, S. Sandfeld and A. Prakash, *Materialia*, 2022, 101314.
- 104 L. A. Gowsalya and M. E. Afshan, *Casting Processes and Modelling of Metallic Materials*, IntechOpen, 2021.